

See discussions, stats, and author profiles for this publication at: <https://www.researchgate.net/publication/306244735>

# Capillary pressure–saturation relations in quartz and carbonate sands: Limitations for correlating capillary and wettability...

Article · August 2016

DOI: 10.1002/2016WR018816

CITATIONS

2

READS

114

5 authors, including:



**Shibo Wang**

Lawrence Berkeley National Laboratory

16 PUBLICATIONS 168 CITATIONS

[SEE PROFILE](#)



**Tetsu K. Tokunaga**

Lawrence Berkeley National Laboratory

183 PUBLICATIONS 3,573 CITATIONS

[SEE PROFILE](#)



**Jiamin Wan**

Lawrence Berkeley National Laboratory

157 PUBLICATIONS 3,251 CITATIONS

[SEE PROFILE](#)



**Yongman Kim**

Lawrence Berkeley National Laboratory

41 PUBLICATIONS 527 CITATIONS

[SEE PROFILE](#)

Some of the authors of this publication are also working on these related projects:



Watershed Function Scientific Focus Area (SFA), Lawrence Berkeley National Lab [View project](#)



Technetium chemistry [View project](#)



## RESEARCH ARTICLE

10.1002/2016WR018816

## Key Points:

- Capillary pressure-saturation relations and residual trapping for multiple fluid systems in quartz and carbonate media were studied
- Wettability alteration causes lower than expected capillary pressures and higher than expected residual trapping of decane and  $\text{scCO}_2$
- Using surrogate fluid underpredicts residual trapping of  $\text{scCO}_2$ . Experiments with  $\text{scCO}_2$  remain necessary to measure capillary behavior

## Supporting Information:

- Supporting Information S1

## Correspondence to:

S. Wang,  
ShiboWang@lbl.gov

## Citation:

Wang, S., T. K. Tokunaga, J. Wan, W. Dong, and Y. Kim (2016), Capillary pressure-saturation relations in quartz and carbonate sands: Limitations for correlating capillary and wettability influences on air, oil, and supercritical  $\text{CO}_2$  trapping, *Water Resour. Res.*, 52, doi:10.1002/2016WR018816.

Received 19 FEB 2016

Accepted 6 AUG 2016

Accepted article online 16 AUG 2016

# Capillary pressure-saturation relations in quartz and carbonate sands: Limitations for correlating capillary and wettability influences on air, oil, and supercritical $\text{CO}_2$ trapping

Shibo Wang<sup>1</sup>, Tetsu K. Tokunaga<sup>1</sup>, Jiamin Wan<sup>1</sup>, Wenming Dong<sup>1</sup>, and Yongman Kim<sup>1</sup>
<sup>1</sup>Energy Geosciences Division, Lawrence Berkeley National Laboratory, Berkeley, California, USA

**Abstract** Capillary pressure ( $P_c$ )-saturation ( $S_w$ ) relations are essential for predicting equilibrium and flow of immiscible fluid pairs in soils and deeper geologic formations. In systems that are difficult to measure, behavior is often estimated based on capillary scaling of easily measured  $P_c$ - $S_w$  relations (e.g., air-water, and oil-water), yet the reliability of such approximations needs to be examined. In this study, 17 sets of brine drainage and imbibition curves were measured with air-brine, decane-brine, and supercritical (sc)  $\text{CO}_2$ -brine in homogeneous quartz and carbonate sands, using porous plate systems under ambient (0.1 MPa, 23°C) and reservoir (12.0 MPa, 45°C) conditions. Comparisons between these measurements showed significant differences in residual nonwetting phase saturation,  $S_{nw,r}$ . Through applying capillary scaling, changes in interfacial properties were indicated, particularly wettability. With respect to the residual trapping of the nonwetting phases,  $S_{nw,r, \text{CO}_2} > S_{nw,r, \text{decane}} > S_{nw,r, \text{air}}$ . Decane-brine and  $\text{scCO}_2$ -brine  $P_c$ - $S_w$  curves deviated significantly from predictions assuming hydrophilic interactions. Moreover, neither the scaled capillary behavior nor  $S_{nw,r}$  for  $\text{scCO}_2$ -brine were well represented by decane-brine, apparently because of differences in wettability and viscosities, indicating limitations for using decane (and other organic liquids) as a surrogate fluid in studies intended to apply to geological carbon sequestration. Thus, challenges remain in applying scaling for predicting capillary trapping and multiphase displacement processes across such diverse fields as vadose zone hydrology, enhanced oil recovery, and geologic carbon sequestration.

## 1. Introduction

Understanding the behavior of multiphase fluid equilibrium and flow in porous geologic formations is needed to better predict fate and transport processes in vadose zone hydrology, geologic carbon sequestration (GCS), and enhanced oil recovery (EOR). Understanding how water and air move within the vadose zone is very important for predictions in agriculture, ecology, groundwater recharge, contaminant transport, and environmental remediation [Faybishenko, 1995; Sakaki et al., 2013; Jost et al., 2015]. GCS in saline reservoirs involves deep injection of carbon dioxide ( $\text{CO}_2$ ) produced in fossil fuel burning electric power plants, and has the potential to substantially reduce rates of increases in atmospheric  $\text{CO}_2$  and is among the most important technologies for mitigating global warming [Intergovernmental Panel on Climate Change, 2005; Benson and Cole, 2008]. At implementation,  $\text{CO}_2$  captured from anthropogenic sources is injected into porous subsurface formations (mostly at depths  $> 800$  m) for storage in its supercritical (sc) state. In EOR, water flooding and  $\text{CO}_2$  flooding of the reservoir are commonly implemented to increase oil recovery after production under in situ reservoir pressure [Yang and Reed, 1989; Enick et al., 2012; Farajzadeh et al., 2012]. Spontaneous imbibition, the process where native brine is drawn into a porous medium under capillarity to displace the oil in place, is dominated by the capillary and wettability characteristics of the reservoir formation. Likewise, the efficacy of water flooding and  $\text{CO}_2$  flooding processes (water or  $\text{CO}_2$  being forced through oil bearing rocks) is strongly affected by capillarity and wettability (and miscibility between  $\text{CO}_2$  and oil for  $\text{CO}_2$  flooding).

Common problems shared between GCS and  $\text{CO}_2$ -EOR operations include nonuniform displacement fronts and buoyancy-driven flow of displacing fluid (i.e.,  $\text{CO}_2$ ). The high mobility of  $\text{CO}_2$  relative to both water and oil, and heterogeneity of the reservoirs and caprocks, makes it very challenging to control the migration of  $\text{CO}_2$  [Enick et al., 2012]. In depth understanding of the capillary and wettability behaviors of geofluid pairs in reservoir formation is a key to improve mobility control and sweep efficiency.

The fate and transport of aqueous (reservoir brine usually being the wetting phase (WP)) and nonaqueous (oil, CO<sub>2</sub>, and air usually as the nonwetting phase (NWP)) fluids including distribution, displacement, and entrapment are complex processes central to these problems. Although many studies have been directed at understanding fundamental mechanisms controlling water and air transport in vadose zone [Haines, 1930; Leverett, 1941; Miller and Miller, 1956; Klute and Wilkinson, 1958; Parker et al., 1987], CO<sub>2</sub> storage [Benson and Cole, 2008; Tokunaga and Wan, 2013; Iglauder et al., 2015; Krevor et al., 2015], oil migration in reservoirs [Yang and Reed, 1989; Enick et al., 2012; Mason and Morrow, 2013], and pore-scale multiphase flow [Celia et al., 1995; Valvatne and Blunt, 2004; Blunt et al., 2013], this remains a challenging area under active research. At the pore scale, interfacial phenomena (capillarity, interfacial tension, and wettability) govern the entrapment of air, CO<sub>2</sub>, and oil. Therefore, understanding the fundamental relations between capillary pressure (pressure of the NWP air/CO<sub>2</sub>/oil relative to the WP brine,  $P_c$ ), brine saturation ( $S_w$ ), wettability (i.e., contact angle,  $\theta$ ), interfacial tension (IFT,  $\gamma$ ), and pore structure is the basis for mechanistic prediction of these important processes. How air and CO<sub>2</sub> become trapped in the pore space on one hand, and how trapped oil is mobilized on the other hand can be better understood through measurements of  $P_c$ - $S_w$  relations for air-brine, scCO<sub>2</sub>-brine and oil-brine systems in well-characterized reservoir media.

The distributions of air/CO<sub>2</sub>/oil and water in the reservoir are location and time-dependent. During drainage, under the influence of the higher pressure in the NWP, air/CO<sub>2</sub>/oil displacement of resident water is controlled by the drainage  $P_c$ - $S_w$  relation of the reservoir media. When the WP pressure increases relative to that of the NWP, air/CO<sub>2</sub>/oil retreat along the separate imbibition (rewetting)  $P_c$ - $S_w$  curves. These capillarity and wettability-driven processes are resisted by viscous/shearing drag and snap-off of NWP ganglia, making the reoccupation of the pores by water incomplete. The retained quantity of air/CO<sub>2</sub>/oil in the pore network constitutes the residual NWP saturation,  $S_{nw,r}$ . Information on  $S_{nw,r}$  is crucial for reliably predicting amounts of air that become trapped in the capillary fringe, CO<sub>2</sub> that can be stored in deep saline aquifers, and oil that can be recovered from reservoir formations.  $S_{nw,r}$  reflects the path and history-dependent (hysteretic) characteristics of the  $P_c$ - $S_w$  relations [Haines, 1930; Mason and Morrow, 2013; Tokunaga et al., 2013; Wang and Tokunaga, 2015]. However, the complex interrelations between porosity, pore geometry and tortuosity, pore-size distribution, wettability, reservoir mineralogy, pore lining materials, fluid properties, geochemistry, and interfacial chemistry make it very challenging to reliably predict the  $P_c$ - $S_w$  relations and  $S_{nw,r}$  across diverse media. Adding to this challenge are incompletely understood pore fluid dynamic phenomena including Haines jumps, thin film flow and snap-off [Roof, 1970; Berg et al., 2013a; Deng et al., 2014].

Scrutiny of capillarity, wettability phenomena, and their synergy is important to improve the understanding of capillary trapping and multiphase displacement processes. At hydrostatic equilibrium, the relationship between  $P_c$ ,  $\gamma$  and  $\theta$  is described by the well-known Young-Laplace equation (equation (1)).

$$P_c = \frac{2\gamma \cos \theta}{R} \quad (1)$$

where  $R$  is the characteristic pore radius associated with the fluid-fluid interface.

In principle,  $P_c$  is the required pressure differential to maintain the curvature of interface between the wetting and nonwetting fluid phases relative to the porous media. As shown in Figure 1, the capillarity-wettability condition governs flow regimes. In a water-wetting geologic media, episodic displacements of menisci (i.e., Haines jumps) and snap-off (i.e., disconnection of the NWP ganglia when passing pore constrictions) are facilitated by the converging-diverging pore geometry [Haines, 1930; Roof, 1970; Berg et al., 2013a; Deng et al., 2014]. The continuity of NWP flow is impeded and the resultant ganglia/blobs/clusters of air/CO<sub>2</sub>/oil constitute  $S_{nw,r}$  [Al Mansoori et al., 2009; Gittins et al., 2010; Krevor et al., 2015]. Conversely, an intermediate-wetting configuration favors a more piston-like displacement regime [Blunt, 1998; Zhao et al., 2010; Al-Menhali and Krevor, 2016]. In such way, the continuity of NWP is maintained. The water film confined between the NWP and pore walls may be thinner, which significantly lowers the ability of brine to counter-flow around and snap off the NWP [Basu and Sharma, 1996; Blunt, 1998; Suicmez et al., 2008; Zhao et al., 2010]. Even if the flow results in disconnected NWP ganglia, some fraction could still migrate in a "ganglia train" and decrease the residual saturation [Yang and Reed, 1989; Farajzadeh et al., 2012]. However, when the thinned water film is unstable and ruptures, air/CO<sub>2</sub>/oil directly contacts the pore walls [Buckley et al., 1989; Basu and Sharma, 1996; Wang et al., 2013]. Contact line pinning/adhesion could ensue which increases the entrapment of the NWP in pores [Kendall, 1994; Hong et al., 2011; Broseta et al., 2012; Wang et al., 2013].

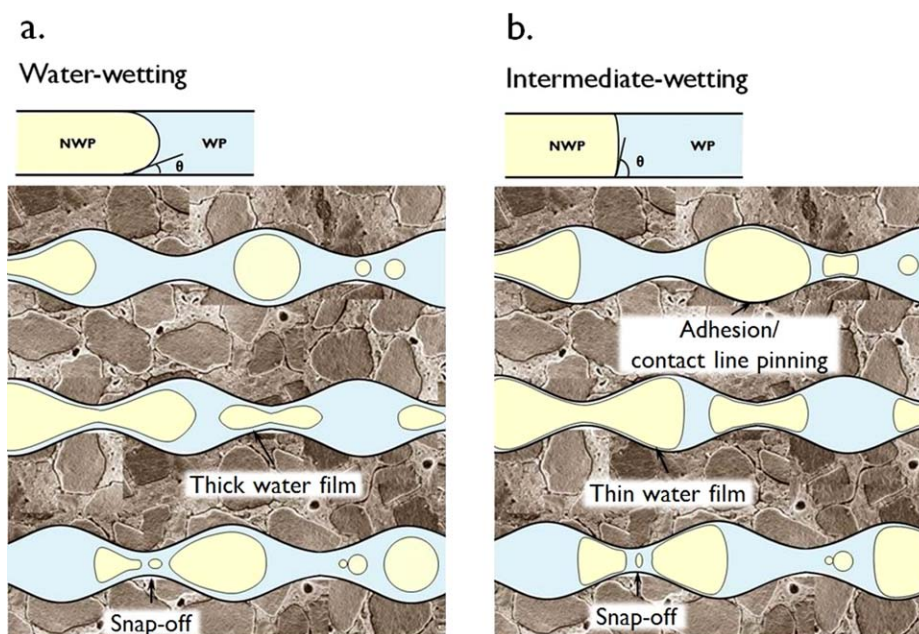


**Figure 1.** Capillarity-wettability configuration determines multiphase displacement regimes. (a) Water-wetting scenario favors Haines jumps and snap-off and therefore tends to entrap greater amount of NWP. In contrast, (b) intermediate-wetting regime facilitates more “piston-like” displacement which reduces  $S_{nw,r}$ . This is, however, complicated by the occurrence of contact line pinning and adhesion which more likely happen with thinning of WP film. These interfacial phenomena strongly immobilize the NWP and increase  $S_{nw,r}$ . Background cemented rock picture was adapted from Hilfer [1996] and modified by the authors.

Residual NWP (e.g.,  $\text{scCO}_2$ , oil, natural gas, air, and  $\text{N}_2$ ) trapping in consolidated cores [Land, 1968; Suzanne et al., 2003; Iglauder et al., 2011; Pini et al., 2012; El-Maghraby and Blunt, 2013; Andrew et al., 2014; Geistlinger et al., 2014; Krevor et al., 2015; Al-Menhali and Krevor, 2016] and unconsolidated sand packs [Plug and Bruining, 2007; Gittins et al., 2010; Tokunaga et al., 2013; Tutolo et al., 2014; Wang and Tokunaga, 2015] have been extensively studied. It is concluded that  $S_{nw,r}$  is dependent on pore network characteristics (e.g., porosity  $\phi$ , relative permeability  $\kappa_r$ , pore-size distribution, heterogeneity) as well as initial NWP saturation,  $S_{nw,i}$ . Models have been developed to correlate  $S_{nw,r}$  with irreducible WP saturation ( $S_{w,ir}$ ),  $S_{nw,ir}$ ,  $\kappa_r$ , and  $\phi$ . Land’s model [Land, 1968] and its recent developments [Kantzas et al., 2001; Suzanne et al., 2003; Gittins et al., 2010] predict  $S_{nw,r}$  well in consolidated porous media and Aissaoui [1983]’s doubly linear relation applies well in unconsolidated porous media.

Attempts have been made to predict  $S_{nw,r}$  of a certain NWP fluids based on the measured behavior of other NWP fluids [Gittins et al., 2010; Pentland et al., 2010; Iglauder et al., 2011; Pini et al., 2012; Tanino and Blunt, 2013]. For example,  $S_{nw,CO_2}$  has been predicted with data on oil, gas, and air at both the macroscopic [Iglauder et al., 2011; Mori et al., 2015] and pore scales [Chaudhary et al., 2013; Andrew et al., 2014]. It has been expected that consolidated porous media generally entrap more NWP in the pores due to more heterogeneous pore structure and wettability conditions. However, contrary experimental results have been reported in consolidated porous media [Al Mansoori et al., 2009; Iglauder et al., 2011; Deng et al., 2014] and in unconsolidated porous media [Plug and Bruining, 2007; Tokunaga et al., 2013; Wang and Tokunaga, 2015], and impacts of pore structure and capillary heterogeneity and mixed wettability remain challenging to predict [Suicmez et al., 2008; Pini et al., 2012; Al-Menhali and Krevor, 2016]. Thus, there remains a need for additional systematic experimental studies using various fluid pairs with different interfacial properties in various porous media with well-defined hydraulic properties. We applied this strategy in order to better understand capillary trapping and the influence of interfacial and fluid properties.

Assessment of capillary trapping in air-brine,  $\text{CO}_2$ -brine, and oil-brine systems is facilitated through measurements of both drainage and imbibition  $P_c$ - $S_w$  relations. In the drainage experiments,  $P_c$  must be large enough for the invading NWP to displace WP menisci through pore throats. A process-specific  $S_{w,ir}$  is reached at the end of drainage. In the subsequent imbibition measurements, a lower  $P_c$  is required for brine

to refill pore bodies, resulting in the hysteresis in capillarity, wettability, and  $S_{nw,r}$ . Notably, advancing and receding  $\theta$  are related to  $P_c$  during imbibition and drainage, respectively. Their relations follow equation (1), which is also the basis for the inferred advancing and receding  $\theta$  from capillary scaling in the later context (equation (3)).

$P_c$ – $S_w$  measurements in porous media analysis are routine, often by using porous plate, core flooding, mercury injection, or centrifuge methods [Leverett, 1941; Parker et al., 1987; Valvatne and Blunt, 2004; Plug and Bruining, 2007; Tokunaga et al., 2013; Wang and Tokunaga, 2015]. Core flooding, recently augmented with X-ray computed tomography (CT), is attractive due to its efficiency and direct visualization of fluid phase distributions. However, most of the core flooding work reported only for the tested drainage processes. Measurements of drainage-imbibition hysteretic loops that include the region with zero  $P_c$  are needed in order to completely assess  $S_{nw,r}$ . In this regard, the porous plate method has advantages [Bull et al., 2011], yet is relatively underutilized, especially to obtain both drainage and imbibition and the resultant  $P_c$ – $S_w$ . Particularly for  $\text{scCO}_2$ , very few direct measurements of drainage and imbibition  $P_c$ – $S_w$  relations are available under representative reservoir conditions [Plug and Bruining, 2007; Iglauer et al., 2011; Pini et al., 2012; Tokunaga et al., 2013; Wang and Tokunaga, 2015]. Among these studies, only Plug and Bruining [2007], Tokunaga et al. [2013], and Wang and Tokunaga [2015] determined  $S_{nw,r,\text{CO}_2}$  during imbibition under controlled  $P_c$ .

Again, the complex effects of interfacial phenomena on the  $P_c$ – $S_w$  relations and  $S_{nw,r}$  remain unclear, as noted in the description of Figure 1. Experiments with multiple pairs of geofluids having different  $\gamma$  and  $\theta$  are useful for examining influences of interfacial properties on the  $P_c$ – $S_w$  relations and  $S_{nw,r}$ . Therefore, the experiments presented here include several fluid pairs in homogeneous quartz and carbonate sandpacks in order to study the above mentioned questions (Table 1).

Capillary scaling has been used to predict equilibrium and flow of immiscible fluids for many decades [Haines, 1930; Leverett, 1941; Miller and Miller, 1956; Klute and Wilkinson, 1958; Parker et al., 1987; Schroth et al., 1996; Plug and Bruining, 2007; Tokunaga et al., 2013; Mori et al., 2015; Wang and Tokunaga, 2015]. The scaled capillary pressure,  $\Pi_c$  (equation (2)) is defined here by assigning the characteristic grain size as the capillary length scale  $\lambda$  to calculate universal drainage and imbibition  $\Pi_c$ – $S_w$  relations which are shared among geometrically analogous porous media (sharing common porosity  $\phi$  and contact angle  $\theta$ ).

$$\Pi_c = \frac{\lambda P_c}{\gamma} \quad (2)$$

**Table 1.** Pressure and Temperature Dependent Fluid and Interfacial Properties Under Our Experimental Conditions

Temperature	°C	23	23	23	45
Pressure	MPa	0.1	0.1	0.1	12.0
Fluid pair		Air-water (#1)	Air-brine <sup>a</sup> (#2)	Decane-brine <sup>a</sup> (#3)	scCO <sub>2</sub> -brine <sup>a</sup> (#4)
Aqueous fluid density, $\rho_w$	kg·m <sup>−3</sup>	998 <sup>b</sup>	1036 <sup>c</sup>	1036 <sup>c</sup>	1034 <sup>c</sup>
Nonaqueous fluid density, $\rho_n$	kg·m <sup>−3</sup>	1.2	1.2	730	658 <sup>b</sup>
$\rho_w - \rho_n$	kg·m <sup>−3</sup>	997	1035	306	376
$(\rho_w - \rho_n)g$	kg·m <sup>−2</sup> ·s <sup>−2</sup>	9781	10,153	3002	3689
$(\rho_w - \rho_n)g(H/2)$	Pa	147 <sup>d</sup>	152 <sup>d</sup>	45 <sup>d</sup>	37 <sup>d</sup>
Interfacial tension, $\gamma$	mN·m <sup>−1</sup>	72.5 <sup>e</sup>	73.2 <sup>e</sup>	48.0 <sup>e</sup>	30.1 ± 0.4 <sup>f</sup>
Aqueous phase viscosity, $\mu_w$	μPa·s	937 <sup>g</sup>	1022 <sup>g</sup>	1022 <sup>g</sup>	662 <sup>g</sup>
Nonaqueous phase viscosity, $\mu_n$	μPa·s	18 <sup>h</sup>	18 <sup>h</sup>	868 <sup>b</sup>	51 <sup>b</sup>
Viscosity ratio, $\mu_n/\mu_w$		0.019	0.018	0.85	0.079

<sup>a</sup>The 1M brine used in this study was synthetic solution prepared by solely adding NaCl.

<sup>b</sup>Water and scCO<sub>2</sub> densities, and scCO<sub>2</sub> and decane viscosities were obtained from the National Institute of Standards and Technology [2016] web-based database (<http://webbook.nist.gov/chemistry/fluid/>).

<sup>c</sup>The NaCl brine densities were calculated based on the regression equations of Batzle and Wang [1992].

<sup>d</sup>The  $(\rho_w - \rho_n)g(H/2)$  values represent variations in  $P_c$  relative to the value at the center of the sandpack, associated with ±0.01 m (half the sample height,  $H = 0.02$  m) for scCO<sub>2</sub> and ±0.015 m ( $H = 0.03$  m) for air and decane under hydrostatic equilibrium condition.

<sup>e</sup>Interfacial tension values for 1.0M NaCl air-brine and decane-brine were measured in our laboratory using the KRÜSS Tensiometer.

<sup>f</sup>Interfacial tension for scCO<sub>2</sub>-brine were measured in our laboratory using the pendant drop method [Bachu and Bennion, 2009].

<sup>g</sup>Water viscosity from Kestin et al. [1981].

<sup>h</sup>Air viscosity was obtained from Lemmon and Jacobsen [2004].

<sup>i</sup>This fluid (12 MPa) was studied in our previous investigations [Tokunaga et al., 2013; Wang and Tokunaga, 2015].



A more general scaling of  $P_c$  further includes the effect of wettability (equation (3)), through matching  $\gamma$  and  $\theta$  scaled curves with the universal scaling drainage and imbibition curves.

$$\frac{\Pi_c}{\cos \theta} = \frac{\lambda P_c}{\gamma \cos \theta} \quad (3)$$

In principle, the Leverett- $J$  function [Leverett, 1941] describes phenomena of the same physical nature as equation (2) and (3) where  $\lambda$  and  $(\kappa/\phi)^{1/2}$  terms may be directly proportional and interchangeable. These practices are less rigorous [Philip, 1971; Anderson, 1987] and can be complicated by contact angle hysteresis, mixed wetting conditions, and other chemical heterogeneities within porous media. To reduce uncertainties in these aspects, our work is restricted to comparing  $P_c$ - $S_w$  relations between air-brine, oil-brine, and scCO<sub>2</sub>-brine fluid systems in homogeneous sandpacks. A large body of literature with air and oil as the NWP is available for comparison with the  $P_c$ - $S_w$  measurements in homogeneous sand obtained here [Haines, 1930; Leverett, 1941; Klute and Wilkinson, 1958; Schroth et al., 1996].

Understanding capillary/residual trapping and quantifying residual saturation of air, scCO<sub>2</sub>, and oil in reservoir are the major incentives of the  $P_c$ - $S_w$  measurements presented here. As described earlier, given the few ambient-condition and reservoir-condition measurements of imbibition and trapping using the porous plate method, and uncertainties/complexities in capillarity and wettability mechanisms, consensus is yet to be reached regarding residual CO<sub>2</sub> trapping in different types of GCS reservoirs (especially sandstone and carbonate rocks), residual oil remaining in reservoirs following EOR, as well as air entrapment in the capillary fringe. Moreover, the validity of predicting capillary trapping of scCO<sub>2</sub> based on the measured behavior of air, oil, and gas is currently uncertain. Thus, there remains a need for comprehensive studies involving testing of various fluid pairs, porous media, experimental conditions, and duration of experiments. Here, equilibrium capillary and NWP entrapment phenomena of oil (decane as analogue)-brine, scCO<sub>2</sub>-brine, and air-brine in quartz and carbonate (limestone and dolomite) sands under ambient and reservoir conditions were systematically studied. It should be noted that decane has also previously been used as an analogue to scCO<sub>2</sub> based on similar properties [Iglauder et al., 2011; Pentland et al., 2011]. Although these studies reported reasonable agreements between capillary behavior of decane-brine and scCO<sub>2</sub>-brine, Berg et al. [2013b] concluded that these fluid pairs differ, with scCO<sub>2</sub>-brine exhibiting intermediate wetting. Therefore, the experiments here with decane as a NWP serve to further explore predictions for both EOR and GCS processes.

## 2. Materials and Methods

Three high-precision  $P_c$ - $S_w$  experimental systems using the semipermeable porous plate technique were built for the three fluid systems, respectively. Particularly for scCO<sub>2</sub>, a semiautomated system was developed and combined with our newly designed high-pressure  $P_c$ - $S_w$  regulator/meter mounted onto a computer programmed linear actuator apparatus. Extensive data were acquired on seventeen groups of repeatedly measured brine drainage and imbibition curves with four fluid pairs for the three fluid systems. These data were then analyzed using capillary scaling to identify possible deviations from assumed wettability and interfacial tension, and to determine  $S_{nw,r}$ .

### 2.1. Porous Media

Sands within a narrow grain size range were selected for this study because they provide well-defined pore size and structure. Quartz sand (density of 2.67 g/cm<sup>3</sup>, Unimin Corp., Le Sueur, MN), limestone sand (density of 2.71 g/cm<sup>3</sup>, Specialty Minerals Corp., Lucerne Valley, CA), and dolomite sand (density of 2.78 g/cm<sup>3</sup>, Specialty Minerals Corp., Canaan, CT) were sieved and the 250–355  $\mu$ m size fraction of each was retained for the experiments.

Pre and postexperiment analyses on mineral samples were conducted. The morphology and surface roughness of the mineral samples was examined using scanning electron microscope (SEM, Zeiss Gemini Ultra-55, Carl Zeiss AG) analysis. Prior to imaging, the sample grains were sputter coated with gold. SEM images showed that limestone sands are angular while quartz sands are well-rounded. Surface roughness of all the samples is at nanometer to micrometer scale. Comparing the pre and postexperiment samples, insignificant changes in morphology or surface roughness were detected.

Mineralogical compositions of the three sands were confirmed using powder X-ray diffraction (XRD) (Smart-Lab X-ray Diffractometer, Rigaku Corp.).  $\text{SiO}_2$ ,  $\text{CaCO}_3$ , and  $\text{CaMg}(\text{CO}_3)_2$  are the dominant mineral contents in these samples, respectively.

Specific surface area analyses were performed on all the mineral samples using the Brunauer, Emmett, and Teller (BET) method. Samples were vacuum-degassed at  $150^\circ\text{C}$  for 3 h to remove moisture and adsorbed gases, followed with BET measurements conducted using Krypton (Kr) as the absorption gas (Autosorb-1 surface area analyzer, Quantachrome Instruments). Surface areas were calculated following the protocol for 5-point BET measurements within the relative pressure range of 0.05–0.3  $P/P_0$ . Results indicated that the carbonate (i.e., limestone and dolomite) sands have almost identical specific surface areas while quartz sand has a specific surface area that is  $\sim 4$  times that of the carbonates. The low specific surface areas, especially for the carbonates suggest that these sands have insignificant internal porosity. The generally much rougher surface micromorphology of the quartz sands is qualitatively consistent with its higher BET surface area.

In order to best preserve the surface properties of these minerals in their natural state, no aggressive physical or chemical treatments (e.g., acetone, ethanol, acid washing, plasma, and sonication) were used. All the experimental minerals were only cleaned several times in deionized (DI) water to remove finer particles and other loosely attached impurities, followed by oven drying at  $110$ – $120^\circ\text{C}$ .

## 2.2. Fluids

In total, three fluid systems, i.e., air-brine, decane-brine, and  $\text{scCO}_2$ -brine and four fluid pairs (Table 1) were included here. Air, n-Decane ( $\text{CH}_3(\text{CH}_2)_8\text{CH}_3$ , anhydrous,  $\geq 99\%$  purity, ACROS Organics), and  $\text{CO}_2$  (99.99% purity, Airgas) were used as the nonaqueous phases in the experiments. DI water (resistivity of  $18.2 \text{ M}\Omega \text{ cm}^{-1}$ , Milli-Q Integral Water Purification System, Millipore Corp.) and a synthetic brine solution of moderately high salinity (1.0M NaCl, ACS grade, VWR Corp.) were used as the aqueous phases. The brine solution was prepared freshly before every experiment. The experiments with air and decane were carried out under room temperature and pressure (RTP, 0.1 MPa,  $23.0 \pm 0.5^\circ\text{C}$ ) and those with  $\text{scCO}_2$  were conducted under elevated temperature and pressure (ETP, 12.0 MPa,  $45.0 \pm 1^\circ\text{C}$ ) conditions of reservoirs for GCS, as listed in supporting information Table S1, and described in detail in previous studies [Tokunaga *et al.*, 2013; Wang and Tokunaga, 2015]. Fluid and interfacial properties under these experimental conditions are listed in Table 1.

In the  $\text{scCO}_2$ -brine experiments, clean liquid  $\text{CO}_2$  from the bottom of a  $\text{CO}_2$  cylinder was fed via the eductor tube into the high-pressure syringe pump (500D HP, Teledyne Isco Corp., rated to 34.5 MPa) and pressurized to its supercritical states under 12.0 MPa (equivalent to reservoir conditions at depths of  $\sim 1.2$  km). The  $\text{scCO}_2$ -brine  $\gamma$  values were measured in our laboratory using the pendant drop method [Bachu and Bennion, 2009] under the same P-T conditions (Table 1). The  $\gamma$  values of the fluid pairs in the RTP experiments were measured using the Du Noüy ring method using a digital force tensiometer (Model K10ST, KRÜSS GmbH). The  $\gamma$  values of the fluid pairs in the ETP experiments were measured using the pendant drop method described in Bachu and Bennion [2009] in our laboratory.

## 2.3. Experimental Conditions

Seventeen groups of experiments were conducted with the four fluid pairs of the three fluid systems and in quartz, limestone, and dolomite sands under RTP and ETP conditions. These conditions are listed in supporting information Table S1.

## 2.4. Experimental Systems

Due to its reliability [Bull *et al.*, 2011], the “hanging water column” method with semipermeable porous plate was used here in the RTP and ETP experiments [Haines, 1930; Tokunaga *et al.*, 2013; Wang and Tokunaga, 2015]. The porous plate only allows passing of the aqueous phase and separates the nonaqueous phase between the sandpack and underlying fluid cavity, enabling establishment of finite  $P_c$  in the sand (Figure 2). In this study, we utilized this method to obtain WP drainage and imbibition (and hence residual NWP trapping) information at hydrostatic equilibrium using three custom-built multistep outflow-inflow experimental systems for air-brine and decane-brine under RTP condition and for  $\text{scCO}_2$ -brine under ETP condition. The design and functionalities of these systems are introduced below.

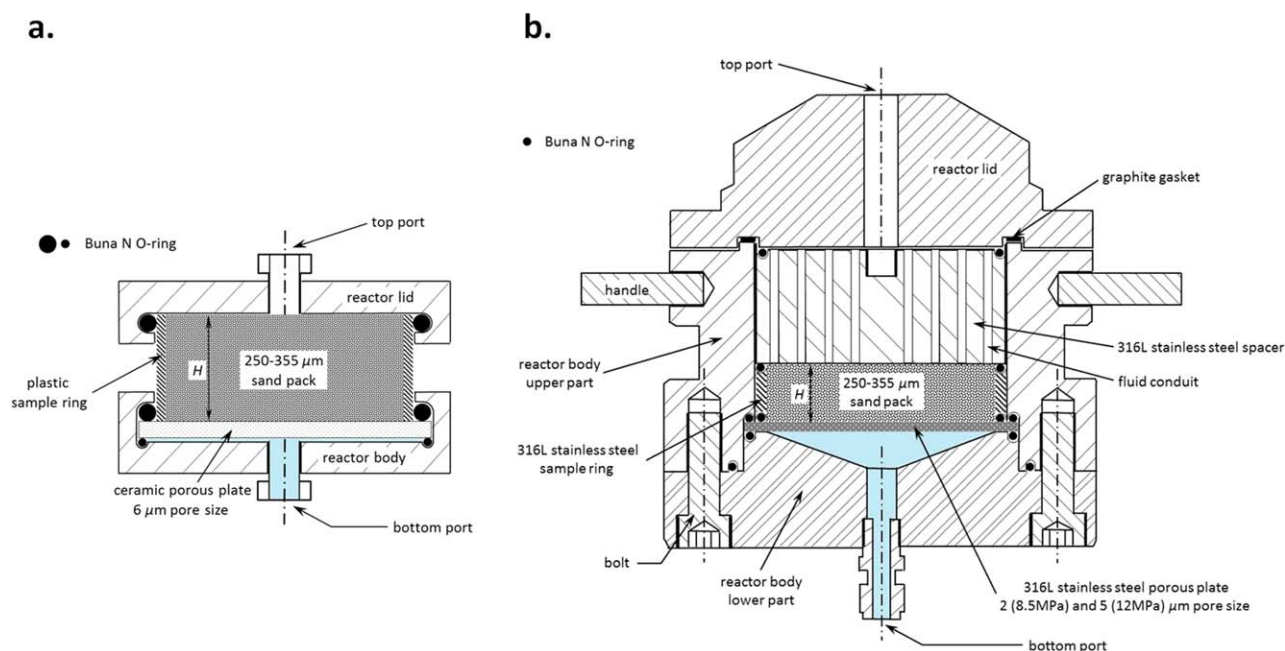


**Figure 2.** (a) Ambient-pressure sample chamber for air-brine and decane-brine experiments (1400 Tempe Pressure Cell with ceramic porous plate, SoilMoisture Equipment Corp.) and (b) high-pressure sample chamber for  $\text{scCO}_2$ -brine experiments (drawing adapted from original drawing by Parr Instrument Co.). A custom-built high-pressure reaction chamber served as the body of the vessel, with additional components placed in its cavity. The reactor lid is sealed into place with bolts on a pair of split ring clamps (not shown).

#### 2.4.1. RTP and ETP Sample Chambers

The configurations of the RTP and ETP sample chambers are shown in Figure 2. In the RTP experiments, the quartz, limestone, and dolomite sand samples resided in a plexiglass chamber (Model 1400 Tempe Pressure Cell, SoilMoisture Equipment Corp.). A porous ceramic plate (0.05 MPa capillary pressure threshold, 12.7 mm thick, 92 mm diameter, Soilmoisture Equipment Corp.) was placed at the bottom of the sample chamber. To minimize air trapping, sand columns were carefully wet-packed to full brine saturation (92 mm diameter, height  $H = 30$  mm,  $\phi = 0.38$ , pore volume 63.0 mL,  $k = 3.9 \times 10^{-11} \text{ m}^2$ ) inside the plexiglass ring on top of the porous plate.

For ETP experiments, the earlier design of the high-pressure sample chamber for  $\text{scCO}_2$  experiments [Tokunaga *et al.*, 2013] was improved, and described in detail in Wang and Tokunaga [2015]. As shown in Figure 2b, the sand column resided inside a custom-designed stainless steel chamber (rated to 20.7 MPa, Parr Instrument Co.). A 316 stainless steel porous plate (2  $\mu\text{m}$  pore-sized plate, 3.0 mm thick, 104.8 mm diameter, Mott Corp.) was fitted into the slot between the upper and lower parts of the sample chamber. A stainless steel ring was placed atop the porous plate. The quartz/limestone sand column was wet-packed with fresh 1.0M brine inside the ring to complete saturation (82.1 mm diameter, height  $H = 20$  mm,  $\phi = 0.38$ , pore volume 42.1 mL,  $k = 3.9 \times 10^{-11} \text{ m}^2$ , hydraulic conductivity  $3.9 \times 10^{-4} \text{ m} \cdot \text{s}^{-1}$ ). A stainless steel spacer (40 mm thick, 94.7 mm diameter, with 24 flow conduits of 3.0 mm diameter) was placed on top of the sandpack to prevent displacement of the column during pressurization and experiments. Housing in the reactor lid, a graphite gasket was used to provide leak-proof sealing and minimize possible contamination. A rupture disc (rated to 20 MPa, Fike Corp.) on the reactor lid ensured safe venting in the event of accidental overpressurization.

It should be noted that short column heights were chosen to (1) minimizing effect of stratified saturation caused by gravity and (2) facilitate equilibration with the porous plate boundary. While more complex flow patterns and saturation distributions could emerge in taller systems, our focus is on determining local equilibrium relations based on macroscopic measurements in homogeneous systems. It is worth mentioning that our experimental cells can in principal be oriented with the short axis horizontal. Such orientation would need measurements of vertical saturation profiles (e.g., tomographically), but would have the advantage of requiring fewer and generally larger boundary  $P_c$  steps because of the broader range of  $P_c$  established along the vertical axis.



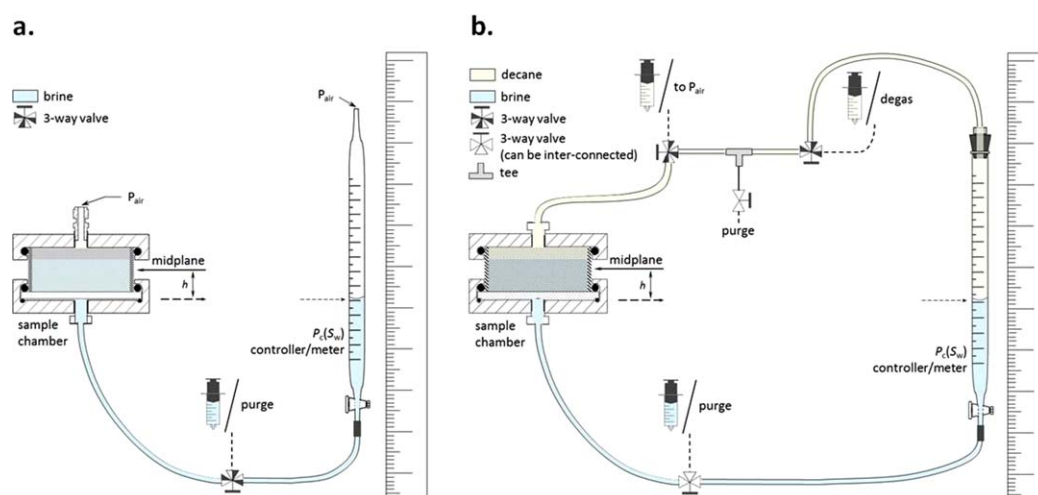


**Figure 3.** RTP  $P_c$ - $S_w$  experimental systems for (a) air-brine and (b) decane-brine. The sandpack's  $P_c$  is controlled by its elevation relative to the nonaqueous phase-brine interface in the  $P_c$ - $S_w$  controller/meter.

#### 2.4.2. RTP Experimental Systems

The RTP  $P_c$ - $S_w$  measuring systems for air-brine and decane-brine are sketched in Figure 3. In the air-brine experiments, the bottom port of the wet-packed sample was connected via polyethylene (PE) tubing to the bottom end of a vertically oriented 100 mL serological pipette (labeled in 1 mL increments, 0.2 mL volume resolution, VWR International Corp.). The pipette served as a  $P_c$  regulator as well as a reservoir for measuring outflow/inflow from/into the porous media sample. The top ports of the column chamber and the pipette were both vented to the room air (and thus local atmospheric pressure). With this configuration,  $P_c$  applied to the sandpack was controlled by adjusting the elevation of the air-brine interface in the pipette relative to the sample center (horizontal midplane) at hydrostatic equilibrium. This configuration allowed for equilibration to a column-averaged  $P_c$ , with a variation within the sandpack of  $\pm(\rho_w - \rho_n)g(H/2)$ , which amounted to  $\pm 147$ – $152$  Pa (Table 1). The sample center was set at 1.5–2 m above the laboratory floor, providing sufficient elevation for reaching  $P_c$  needed to drain the wetting phase to relatively low saturations.

As shown in Figure 3b, the decane-brine experimental system was for the most part similar to the air-brine apparatus except for the added loop section (1/4 inch Teflon tubing, VWR International Corp.) for decane. System assembly, decane injection, and air degassing processes required greater care. The two phase decane-brine displacement utilized a closed-loop configuration with decane (less dense phase) above brine. A 100 mL glass burette (1 mL graduation, 0.2 mL volume resolution, VWR International Corp.) with a custom-made connection unit on top was used as the  $P_c$ - $S_w$  controller/meter. After decane addition into the upper portion of the closed system, air was carefully removed to assure fluid and pressure continuity using decane-filled gas tight syringes. Following the degassing, the system was briefly vented to room air to ensure the whole system was subject to atmospheric pressure by quickly opening and shutting the valve at the highest elevation of the system (to avoid reentering of air). The  $P_c$  variation within the sandpack amounted to  $\pm 45$  Pa (Table 1). The sample center was set at  $\sim 2$  m above ground and the total height of the system reached  $\sim 3.5$  m. An Aluminum-rod network was built to support the hanging decane loop (not shown in the schematic).

#### 2.4.3. ETP Experimental System

In principle, the mechanism of operation for the ETP system is identical to the RTP systems except for the technical challenges such as maintenance of elevated pressure and temperature over long experimental period, control of finite  $P_c$  under high system pressures, fluid flushing, and backpressure control. In the fine-tuned  $\text{scCO}_2$  experimental system (Figure 4), the  $P_c$ - $S_w$  controller/meter simply consisted of a high-pressure sight glass (30 mL capacity, 34.5 MPa rated, Series T-40, Jerguson) with a volumetric graduation superimposed on its tempered glass window. The sight glass was mounted on a computer programmed linear actuator (0.1 mm height resolution, ER50, Parker Hannifin Corp.). This design allows for precise control of  $P_c$  by setting the level of the  $\text{scCO}_2$ -brine interface in the  $P_c$ - $S_w$  controller/meter via the linear actuator at the desired heights below or above the sample (the practical maximum height is about 1.5 m, which was adequate for conditions investigated here). This configuration circumvented the difficulty and instabilities of

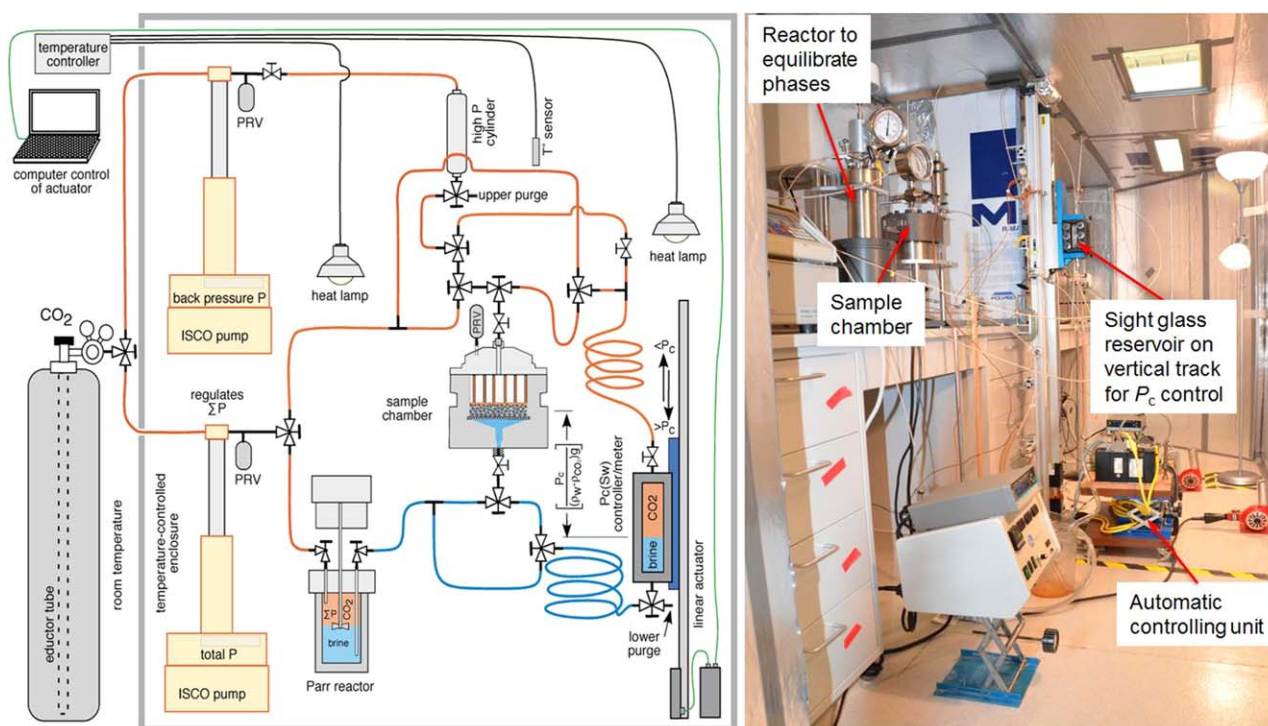


**Figure 4.** ETP  $P_c$ - $S_w$  experimental setup for  $scCO_2$ -brine: (left) schematic and (right) interior of the system. The sample's  $P_c$  was regulated by its elevation relative to the  $scCO_2$ -brine interface in the high-pressure  $P_c$ - $S_w$  controller/meter, which moved vertically under control of a precise computer programmed linear actuator. Pressure relief valves (PRV) are located at the pump and on the sample chamber cap. Experiments were conducted within a constant temperature enclosure. This diagram is revised from Wang and Tokunaga [2015].

regulating  $P_c$  using separate pressure controllers for two fluid phases.  $P_c$  and  $S_w$  can be controlled to very fine resolution ( $<10$  Pa and 0.03, respectively), while maintaining the total pressure at any selected value safely containable by the system [Wang and Tokunaga, 2015].  $P_c$  variations within the column were as large as  $\pm 37$  Pa relative to the midplane value under the influences of gravity and fluid densities (Table 1).

The sight glass' upper and lower ports were connected to the main syringe pump and the sample chamber's upper port (brine-saturated  $scCO_2$ ) and the sample chamber's lower port ( $scCO_2$ -saturated brine), respectively. The upper ports of the sample chamber and sight glass were also connected with a high-pressure cylinder (316L stainless steel, 150 mL, 34.5 MPa rated, Swagelok Co.) for the initial flushing of sandpack and sight glass with  $scCO_2$ -saturated brine. The cylinder was back-pressured at a slightly lower level (0.01–0.05 MPa) than the system pressure with a secondary syringe pump of the same type. Several high-pressure ball and needle valves (17.2 MPa rated, Swagelok) were included in the loop to control fluid flow. The main components of the system were connected via stainless steel and flexible polyetheretherketone (PEEK<sup>TM</sup>) tubing.

Constant-temperature control was important during the months-long  $P_c$ - $S_w$  experiments. This was achieved by housing the whole system inside a custom built thermally insulated, temperature-regulated enclosure at  $45.0 \pm 1^\circ\text{C}$  (Figure 4). The system's temperature was maintained by convective heating with four 250 W infrared halogen lamps.

## 2.5. Experimental Procedures

Prior to experiments, the equipment including the syringe pumps, the high pressure cylinder, the sight glass vessel, the porous plates, the sample chambers, valves, connectors, tubing, and all the other components were cleaned with acetone/ethanol first, then extensively rinsed with DI water and finally flushed with clean compressed air. The data collection of a complete drainage/imbibition curve takes 3–4 weeks (i.e., 1.5–2 months for a full drainage-imbibition cycle).

### 2.5.1. RTP Experiments

Before experiment, the whole system was meticulously checked for trapped air. Degassing operations were repeated when necessary. The brine level in the pipette/burette was adjusted to a position within the

bottom portion of the pipette/burette (low volume reading), and hydrostatically equilibrated at the center of the sandpack for at least 24 h before measurements ensued.

Drainage experiments were conducted by successively moving the air-brine/decane-brine interface in the pipette/burette downward to lower elevations and quantifying outflow volumes. Imbibition measurements were performed by reversing the procedure through a series of stepwise equilibrations upward, eventually returning to zero  $P_c$ . One to two day equilibration times were given between steps. Duplicate/secondary cycles of drainage and imbibition followed the primary ones.

### 2.5.2. ETP Experiments

To ensure safety, as many preparatory steps as possible were performed at room temperature. The later initialization and adjustment steps conducted by working within the thermal enclosure were done quickly to avoid heat-related health risks.

Before experiments, about 350 mL fresh brine was added into a high-pressure stirred reactor vessel (450 mL capacity, rated to 20 MPa, 4562 Mini Reactor system, Parr Instrument Co.). The  $\text{scCO}_2$  in the syringe pump was then injected into the stirred reactor to prepare brine-saturated  $\text{scCO}_2$  and  $\text{scCO}_2$ -saturated brine.  $\text{scCO}_2$  and brine were mixed for at least 48 h to reach phase equilibrium. Prevention of leakage during these months-long experiments is critical. Therefore, a leak test was meticulously conducted to ensure a leak-proof system before every new experiment.

The operation of the ETP experiments followed the protocol and procedure described in previous studies [Tokunaga *et al.*, 2013; Wang and Tokunaga, 2015] and was not elaborated in detail here. Two (three for experimental condition #17) replicate drainage-imbibition cycles were run. The experiments started with fresh quartz/limestone sands. The ETP experiments were only conducted on quartz and limestone and not dolomite sand because the  $P_c$ - $S_w$  results at RTP showed indiscernible differences between the two carbonate minerals (Figure 5). During drainage, the sight glass was moved downward via the digital actuator to set the  $\text{scCO}_2$ -brine meniscus to a lower elevation (typically by 10 mm) for equilibration at a new  $P_c$ . Similar stepwise operations were taken to progressively get brine drained from the sandpack until further brine removal with increased  $P_c$  became negligible, defining the  $S_{w,ir}$ . At each step, the equilibrated elevation of the meniscus in the sight glass and the outflow volume of brine were recorded. 1 to 2 days were allowed between equilibration steps to assure hydrostatic equilibrium. The imbibition procedure followed, with the sight glass being sequentially raised until the system returned to zero  $P_c$ . Owing to residual  $\text{CO}_2$  trapping,

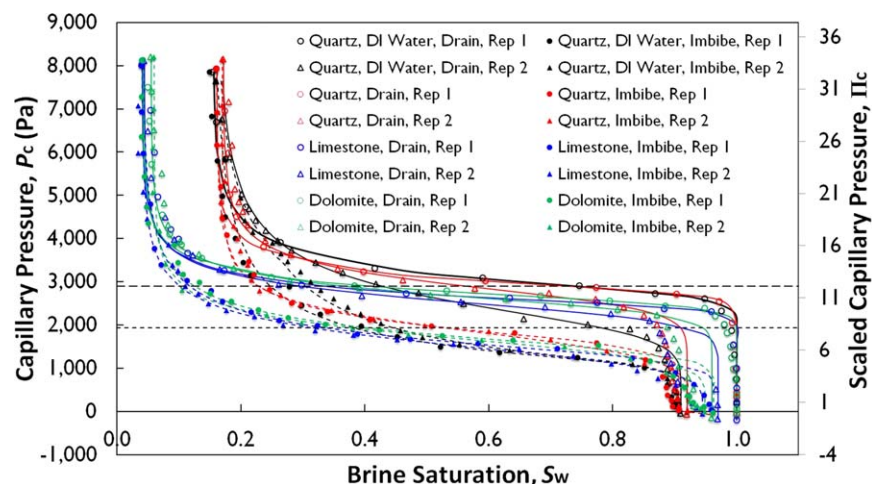


**Figure 5.**  $P_c$ - $S_w$  relations for air-brine system during drainage and imbibition in quartz and carbonate (limestone and dolomite) sands at RTP. The scattered points are experimental data and the continuous curves are the fitted data based on van Genuchten model [van Genuchten, 1980] in the nonlinear regression analysis. The curve fitting parameters are listed in supporting information Table S2. Duplicate cycles of drainage-imbibition experiments were consecutively conducted for each case. The plot includes the unscaled  $P_c$ - $S_w$  and capillary-scaled  $\Pi_c$ - $S_w$  relations ( $\Pi_c = \lambda P_c / \gamma$ ). Universal values of  $\Pi_c$  inflection points ( $\sim 12$  for drainage and  $\sim 8$  for imbibition) are included for comparison and noted by the straight dash lines.  $\gamma$  values listed in Table 1 are used in capillary scaling. "Rep" = Replicate. Consistent symbol conventions are used in all the figures. Specifically, the hollow symbols represent the data of drainage and the filled ones represent the data of imbibition. Circle symbols represent the initial replicate and triangle symbols represent the duplicate replicate (square symbols for the tertiary replicate in  $\text{scCO}_2$ ). Data for quartz, limestone, and dolomite are marked in red, blue, and green, respectively.

full brine saturation was not achieved when returning to zero  $P_c$ . The  $S_{nwr,CO_2}$  information was obtained from the difference in the summed volumes between the drained and imbibed brine. A secondary (and tertiary for experimental condition #17) drainage-imbibition cycle followed the primary one. In order to start with full brine saturation, the flushing procedures were repeated prior to the replicate runs.

### 3. Results and Discussion

In Figures 5–7, we plot experimental results of drainage and imbibition  $P_c$ – $S_w$  relations with  $P_c$  as the dependent variable in terms of  $P_c(S_w)$  and  $P_c(\Theta)$  ( $\Theta = \phi S_w$ , the volumetric brine content). The data are presented in unscaled (measured) and scaled forms. Scaling is first done with  $\lambda$  and  $\gamma$  as  $\Pi_c(S_w)$  and  $\Pi_c(\Theta)$ , and then with  $\lambda$ ,  $\gamma$  and  $\theta$  as  $\Pi_c(S_w)/\cos\theta$  and  $\Pi_c(\Theta)/\cos\theta$ .  $P_c$  and  $\Pi_c$  values are plotted on the primary and secondary vertical axes of the figures, respectively. The data points represent measurements, and the continuous curves are fits to the *van Genuchten* model (equation (4)) used for the nonlinear regression analysis:

$$\Theta(P_c) = \Theta_r + (\Theta_s - \Theta_r) \left[ \frac{1}{1 + (\alpha P_c)^n} \right]^m \quad (4)$$

where  $\Theta_s$  and  $\Theta_r$  are highest and lowest brine contents obtained in a specific drainage or imbibition run, and  $\alpha$ ,  $m$ , and  $n$  are fitting parameters [*van Genuchten*, 1980].  $\Theta_s$  and  $\Theta_r$  are calculated based on the corresponding measured values of brine saturation  $S_s$  and  $S_r$  by multiplying porosity. These curve fitting parameters for different experiments are listed in supporting information Table S2.

For air-brine fluid system,  $P_c$ – $S_w$  relations during drainage and imbibition at RTP in quartz and carbonate (limestone and dolomite) sands were measured in the experimental system shown in Figure 3a. The experimental data are presented in Figure 5. Prior to experiment, the sandpacks were saturated with brine ( $S_{w,i} = 1.0$  and  $\Theta_{w,i} = 0.38$ ). Duplicate cycles of drainage-imbibition experiments were consecutively conducted for each case. Results exhibit reproducibility between the duplicate measurements in all cases. Comparing the results of quartz sand in brines of different salinity (DI water versus 1M NaCl brine),  $P_c$ – $S_w$  behavior is very similar during drainage while major imbibition happens at slightly higher  $P_c$  with increased salinity.  $S_{w,ir}$  and  $S_{nw,r}$  values are almost identical ( $S_{w,ir}$  of 0.15–0.17 ( $\Theta_{w,ir}$  of 0.059–0.065);  $S_{nw,r}$  of 0.08–0.09 ( $\Theta_{nw,r}$  of 0.030–0.035)). For the carbonate species, differences in the  $P_c$ – $S_w$  behaviors are insignificant between limestone and dolomite sands. Consistent  $S_{w,ir}$  and  $S_{nw,r}$  values were obtained ( $S_{w,ir}$  of 0.04–0.06 ( $\Theta_{w,ir}$  of 0.015–0.021);  $S_{nw,r}$  of 0.04–0.06 ( $\Theta_{nw,r}$  of 0.015–0.023)). These similarities in the trend and magnitude of data shared between the limestone and dolomite sands simplify the investigation of the  $P_c$ – $S_w$  relations in carbonate minerals. Based on this similarity,  $P_c$ – $S_w$  experiments were conducted on limestone sand

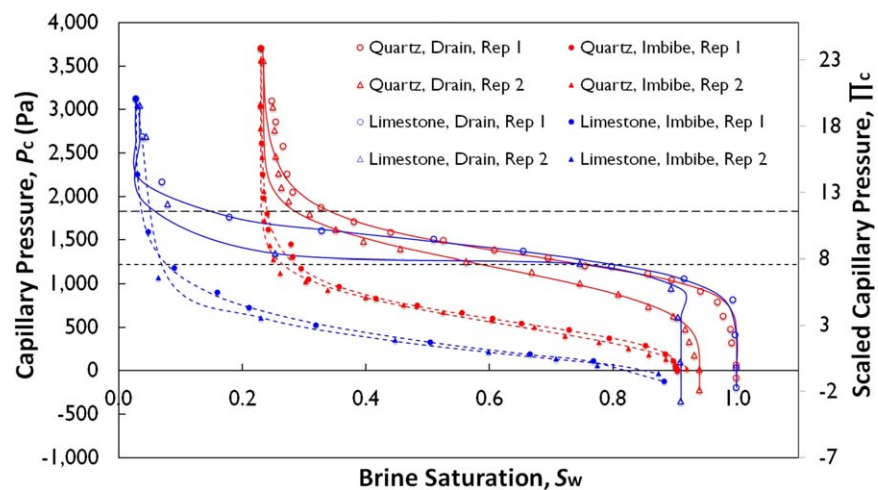


**Figure 6.**  $P_c$ – $S_w$  relations for decane-brine system during drainage and imbibition in quartz and carbonate (limestone) sands at RTP. The discrete data points are experimental data and the continuous curves are the fitted data based on van Genuchten model [*van Genuchten*, 1980]. The curve fitting parameters are listed in supporting information Table S2. Two replicate cycles of drainage-imbibition experiments were conducted for each case. Both the unscaled  $P_c$ – $S_w$  and capillary-scaled  $\Pi_c$ – $S_w$  relations are plotted. Universal scaling inflections (noted by the straight dash lines) are included for comparison. The  $\gamma$  value used in the capillary scaling is listed in Table 1. “Rep” = Replicate.



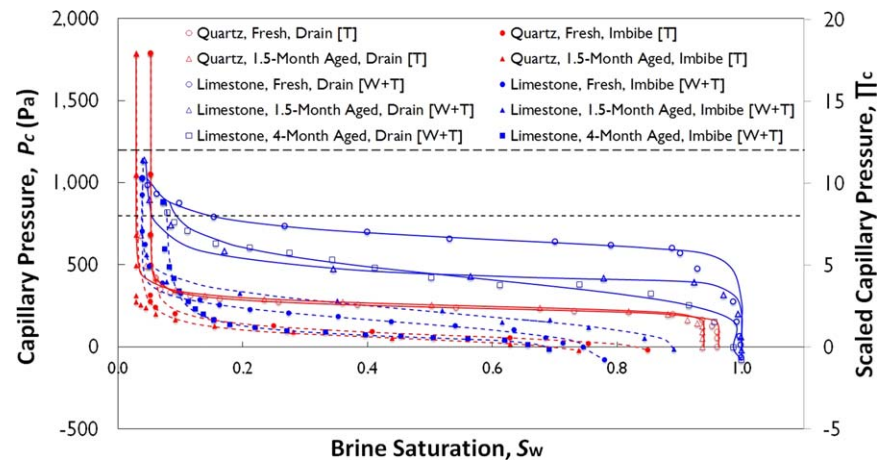


**Figure 7.**  $P_c$ - $S_w$  relations during drainage and imbibition in quartz and limestone sands for  $\text{scCO}_2$ -brine system at 12.0 MPa and 45°C. Capillary-scaled  $\Pi_c$  dependence on brine saturation (data fit with the van Genuchten model [van Genuchten, 1980], values of  $\lambda$  and  $\gamma$  used in capillary scaling listed in Table 1, fitting parameters presented in supporting information Table S2.) was also presented with universal scaling inflections (straight dash lines) included for comparison. The data in this figure were from our previous studies [Tokunaga et al., 2013; Wang and Tokunaga, 2015] and were denoted as [T] and [W + T].

only in the decane-brine and  $\text{scCO}_2$ -brine systems to represent the common physicochemical behaviors of carbonate species. The low  $S_{nw, \text{air}}$  values are anticipated behavior for hydrophilic homogeneous sandpacks [Schroth et al., 1996; Gittins et al., 2010]. Comparing sandstone and carbonate species,  $S_{w, \text{ir}}$  values for limestone and dolomite sands are much lower than those for quartz sand. This is attributed to the geometrical effects that the more angular and smooth carbonate sands retain a thinner water film compared to the more rounded and rough quartz sand.

Quantitative comparisons between capillary scaling predictions and the measured  $P_c$ - $S_w$  relations were made. In Figure 6,  $\Pi_c$  values were calculated with  $\gamma$  (Table 1) and  $\lambda$  (302  $\mu\text{m}$ , median of the 250–355  $\mu\text{m}$  grain size interval retained from sieving the 40/60 sands) to examine whether the major inflections in drainage and imbibition curves can be predicted by  $\gamma$  and  $\lambda$  alone. For homogeneous and hydrophilic sands, inflection values of  $\Pi_c$ - $S_w$  curves are well constrained around 12 for drainage and around 8 for imbibition (straight dash lines in Figure 5–10), respectively [Haines, 1930; Miller and Miller, 1956]. For air-water/brine, most of the scaled drainage and imbibition  $\Pi_c$ - $S_w$  curves are generally in good agreement with the predicted  $\Pi_c$  inflection points for homogeneous sands, while in a few cases, the scaled curves have  $\Pi_c$  inflections slightly lower than predicted. These deviations indicate slightly larger advancing and receding contact angles (Table 2) than predicted based on the assumption of complete hydrophilic interaction. Despite the deviations, the results collectively indicate that the sandstone and carbonate sands are hydrophilic in nature with the air-brine fluid system.

For the decane-brine system, the  $P_c$ - $S_w$  relations during drainage and imbibition at RTP in sandstone (quartz) and carbonate (limestone) sands were measured using the closed-loop porous plate experimental system shown Figure 4b. To our knowledge, this study is the first to characterize  $P_c$ - $S_w$  relations for decane-water fluid system using a custom-designed porous plate system. Two replicate cycles of drainage and imbibition were conducted sequentially. The initial drainage replicate started with complete brine saturation, and ended when  $S_{w, \text{ir}}$  was reached. An imbibition procedure followed until  $P_c$  was reset to its zero level. After imbibition,  $P_c$  was further increased to achieve highest possible brine saturation (as close to  $S_{w, \text{i}} = 1.0$  as possible) to start the duplicate drainage measurements.

As shown in Figure 6, good reproducibility was achieved in all the experiments.  $S_{w, \text{ir}}$  and  $S_{nw, \text{r}}$  values are very similar between replicates for all the quartz and limestone curves. While limestone sand reached much lower  $S_{w, \text{ir}}$  values ( $S_{w, \text{ir}}$  of 0.03,  $\Theta_{w, \text{ir}}$  of 0.012) relative to  $S_{w, \text{ir}}$  in the quartz sand of 0.23 ( $\Theta_{w, \text{ir}}$  of 0.087),  $S_{nw, \text{r}}$  values of the two mineral species are not as different.  $S_{nw, \text{r}}$  of 0.15 to 0.18 ( $\Theta_{nw, \text{r}}$  of 0.051 to 0.060) were obtained for limestone, and  $S_{nw, \text{r}}$  of 0.08–0.10 ( $\Theta_{nw, \text{r}}$  of 0.030–0.036) were obtained for quartz. As previously noted, the more angular shape and smooth surfaces of the limestone sand apparently supports less residual



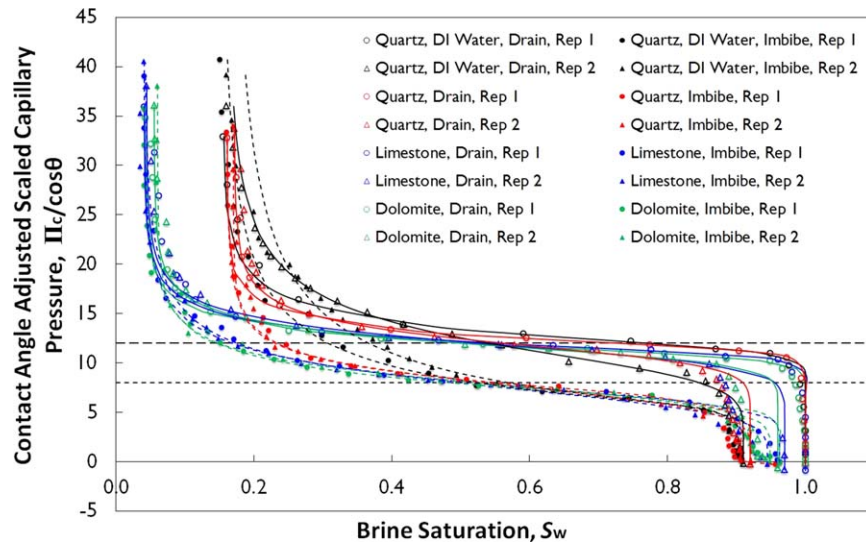


**Figure 8.** Dependence of scaled capillary pressure  $\Pi_c/\cos\theta$  with  $\lambda$ ,  $\gamma$ , and  $\cos\theta$  on brine saturation during drainage and imbibition for air-brine system in quartz and carbonate (limestone and dolomite) sands at RTP. The scaling curves were fit through the characteristic inflection points ( $\sim 12$  for drainage and  $\sim 8$  for imbibition) by adjusting  $\cos\theta$  for drainage and imbibition curves, respectively. The fitted  $\cos\theta$  values and the calculated advancing and receding  $\theta$  values are listed in Table 2. Estimated advancing/receding (drainage/imbibition)  $\theta$  values are  $35^\circ\text{--}36^\circ/0^\circ\text{--}27^\circ$  (quartz with DI water),  $7^\circ\text{--}10^\circ/0^\circ$  (quartz with brine),  $32^\circ\text{--}34^\circ/23^\circ\text{--}28^\circ$  (limestone with brine), and  $20^\circ\text{--}27^\circ/15^\circ\text{--}20^\circ$  (dolomite with brine), respectively.

water than the quartz sand. There is indiscernible difference between replicate cycles, indicating insignificantly time effects on the capillarity and wettability behaviors.

Additional information from the capillary scaling analysis ( $\Pi_c\text{--}S_w$  curves) is shown in Figure 6 (secondary vertical axis). The universal scaling inflection values are denoted with the horizontal dash lines (again,  $\sim 12$  for drainage and  $\sim 8$  for imbibition). Both groups of drainage and imbibition curves for quartz and limestone sands significantly deviate (toward lower  $P_c$ ) from the universal  $\Pi_c$  inflections. Given that  $\gamma$  is well constrained at the decane-brine interface (confirmed with postexperiment measurement), these deviations

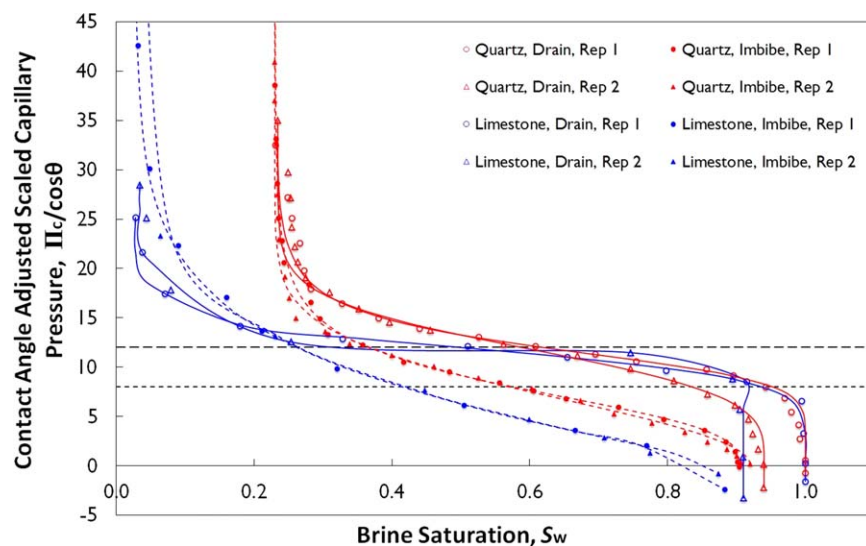


**Figure 9.** Dependence of scaled capillary pressure  $\Pi_c/\cos\theta$  with  $\lambda$ ,  $\gamma$ , and  $\cos\theta$  on brine saturation during drainage and imbibition for decane-brine system in quartz and limestone sands at RTP. The scaling curves were fit through the characteristic inflection points ( $\sim 12$  for drainage and  $\sim 8$  for imbibition) by adjusting  $\cos\theta$  for drainage and imbibition curves, respectively. The fitted  $\cos\theta$  values and the calculated advancing and receding  $\theta$  values are listed in Table 2. Estimated advancing/receding (drainage/imbibition)  $\theta$  values are  $60.5^\circ\text{--}62^\circ/44.5^\circ\text{--}50.4^\circ$  (quartz) and  $70.7^\circ\text{--}73.3^\circ/39^\circ\text{--}47.9^\circ$  (limestone), respectively.

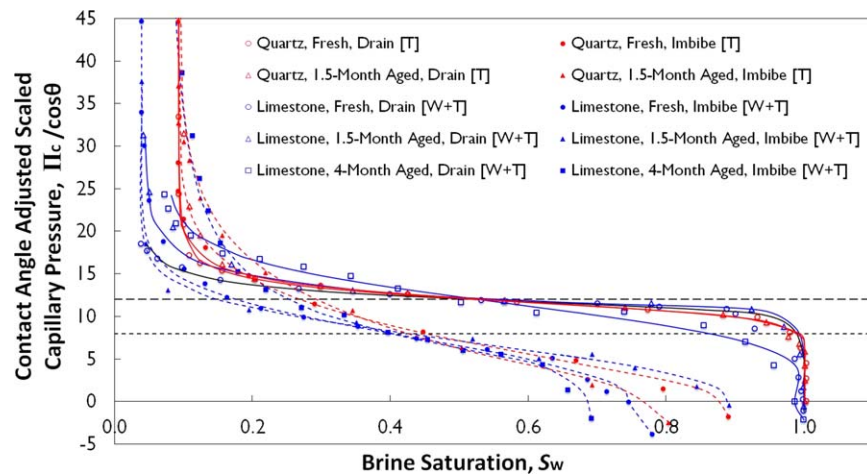


**Figure 10.** Dependence of scaled capillary pressure  $\Pi_c / \cos\theta$  with  $\lambda$ ,  $\gamma$ , and  $\cos\theta$  on brine saturation during drainage and imbibition for  $\text{scCO}_2$ -brine system in quartz and limestone sands at 12.0 MPa and 45°C. The scaling curves were fit through the characteristic inflection points ( $\sim 12$  for drainage and  $\sim 8$  for imbibition) by adjusting  $\cos\theta$  for drainage and imbibition curves, respectively. The fitted  $\cos\theta$  values and the calculated advancing and receding  $\theta$  values are listed in Table 2. Estimated advancing/receding (drainage/imbibition)  $\theta$  values are 83.1°–84.8°/76.5°–77.3° (quartz) and 72.3°–85°/56°–68.6° (limestone), respectively.

imply that decane does not wet quartz and carbonate sands as well as water (measurable wettability indicators listed in Table 2). Contrary results with samples being water wet after contacting with decane-brine were reported [Berg et al., 2013b]. The difference in results may be due to much shorter-time period of experiment and different porous media.

For the  $\text{scCO}_2$ -brine system, we integrated the experimental data from our previous studies which separately investigated  $P_c$ - $S_w$  behaviors in quartz sands [Tokunaga et al., 2013] and carbonate sands [Wang and Tokunaga, 2015] to compare the difference in capillary behavior in these two important reservoir mineral classes. Two successive drainage-imbibition cycles were conducted on quartz sand and three successive cycles were performed on limestone sand (one more replicate cycle to better investigate the exposure time effect of  $\text{scCO}_2$  on interfacial properties that emerged during the first two replicates). Single drainage or imbibition curve took about 4 weeks to complete, a time scale that is comparable with other studies in the literature [Bull et al., 2011]. All together, the experiments for quartz sand took about 4 months, and those for limestone sand took about 6 months. To our knowledge, these studies were the only ones that reported time-lapsed capillarity and wettability phenomena under elevated temperature and pressure conditions at the experimental time scale of several months.

Different from the air-brine and decane-brine experiments, all drainage experiments started at complete saturation with  $\text{scCO}_2$ -saturated brine ( $S_{w,i} = 1.0$ ). The full WP saturation was achieved by flushing the sandpacks with  $\text{scCO}_2$ -saturated brine (2–3 pore volumes) through careful coordination between the main pump and the back-pressure pump (Figure 4). The measured drainage and imbibition  $P_c$ - $S_w$  relations in quartz and limestone sands at 12.0 MPa and 45°C are shown in Figure 7. Also presented are capillary-scaled  $\Pi_c$ - $S_w$  relations with Haines' universal scaling inflections (horizontal dash lines) included for comparison. Both groups of  $P_c$ - $S_w$  and  $\Pi_c$ - $S_w$  curves were fit through a nonlinear regression relation of the van Genuchten model [van Genuchten, 1980]. The data of  $\gamma$  and  $\lambda$  used in capillary scaling are listed in Table 1.

As shown in Figure 7,  $P_c$  curves of quartz and limestone sands all deviate from the universal scaling inflections, with quartz sand curves shifting more significantly. The trends of data were well reproducible in the quartz sand experiments, while the reproducibility of the limestone sand data was not as good. Pronounced time dependence manifested from the three repeatedly measured drainage-imbibition cycles in limestone sandpacks but was less from the two cycles in quartz sand. The  $P_c$ - $S_w$  curves shifted toward lower  $P_c$  with increasing exposure time of  $\text{scCO}_2$ -brine contacting the limestone material. The capillary entry pressure  $P_{c,\text{entry}}$ , the capillary pressure during main drainage  $P_{c,\text{drain}}$ , and the capillary pressure during main imbibition  $P_{c,\text{imbibition}}$  dropped from  $\sim 600$  to  $\sim 200$  Pa, from  $\sim 700$  to  $\sim 500$  Pa, and from  $\sim 200$  to  $\sim 100$  Pa during the 6

**Table 2.** Calculated  $\cos\theta$  and  $\theta$  Values That Fit the Scaled Capillary Pressure  $\Pi_c/\cos\theta$  Through the Universal Scaling Inflections at RTP and ETP (12.0 MPa, 45°C)

		Advancing/Receding Contact Angle $\theta$ , °	$\cos\theta$
Air—water—quartz—1 (#1) <sup>a</sup>	Drainage (receding)	0.0	1.00
	Imbibition (advancing)	36.0	0.81
Air—water—quartz—2 (#2) <sup>a</sup>	Drainage (receding)	27.0	0.89
	Imbibition (advancing)	35.0	0.82
Air—brine—quartz—1 (#3) <sup>a</sup>	Drainage (receding)	0.0	1.00
	Imbibition (advancing)	10.0	0.98
Air—brine—quartz—2 (#4) <sup>a</sup>	Drainage (receding)	0.0	1.00
	Imbibition (advancing)	7.0	0.99
Air—brine—limestone—1 (#5) <sup>a</sup>	Drainage (receding)	23.0	0.92
	Imbibition (advancing)	32.0	0.85
Air—brine—limestone—2 (#6) <sup>a</sup>	Drainage (receding)	28.0	0.88
	Imbibition (advancing)	34.0	0.83
Air—brine—dolomite—1 (#7) <sup>a</sup>	Drainage (receding)	15.0	0.97
	Imbibition (advancing)	20.0	0.94
Air—brine—dolomite—2 (#8) <sup>a</sup>	Drainage (receding)	20.0	0.94
	Imbibition (advancing)	27.0	0.89
Decane—brine—quartz—1 (#9) <sup>a</sup>	Drainage (receding)	44.5	0.71
	Imbibition (advancing)	60.5	0.49
Decane—brine—quartz—2 (#10) <sup>a</sup>	Drainage (receding)	50.4	0.64
	Imbibition (advancing)	62.0	0.47
Decane—brine—limestone—1 (#11) <sup>a</sup>	Drainage (receding)	39.0	0.78
	Imbibition (advancing)	70.7	0.33
Decane—brine—limestone—2 (#12) <sup>a</sup>	Drainage (receding)	47.9	0.67
	Imbibition (advancing)	73.3	0.29
12.0 MPa CO <sub>2</sub> —brine—quartz—1 (#13) <sup>a</sup>	Drainage (receding)	77.3	0.22
	Imbibition (advancing)	83.1	0.12
12.0 MPa CO <sub>2</sub> —brine—quartz—2 (#14) <sup>a</sup>	Drainage (receding)	76.5	0.23
	Imbibition (advancing)	84.8	0.09
12.0 MPa CO <sub>2</sub> —brine—limestone—1 (#15) <sup>a</sup>	Drainage (receding)	56.0	0.56
	Imbibition (advancing)	78.0	0.21
12.0 MPa CO <sub>2</sub> —brine—limestone—2 (#16) <sup>a</sup>	Drainage (receding)	68.6	0.36
	Imbibition (advancing)	72.3	0.30
12.0 MPa CO <sub>2</sub> —brine—limestone—3 (#17) <sup>a</sup>	Drainage (receding)	68.6	0.36
	Imbibition (advancing)	85.0	0.09

<sup>a</sup>The numbers in the parenthesis correspond to the experimental conditions listed in supporting information Table S1.

month experimental period, respectively. We hypothesize that the deviations from the universal scaling inflections were mainly caused by wettability alteration of the porous media, becoming more intermediate wetting over time. This trend was also reported in scCO<sub>2</sub>-brine contacting the Berea sandstone material in a shorter-term experiments [Berg et al., 2013b], and described in our recent papers [Tokunaga et al., 2013; Wang and Tokunaga, 2015]. Greater  $P_c$  hysteresis (also wettability hysteresis) occurred in limestone sand than in quartz sand. This observation is consistent with the fact that in the carbonated brine of pH~3, CO<sub>2</sub> has greater affinity at the molecular level with carbonate species compared to silica species. The known contact

line pinning and CO<sub>2</sub> adhesion with carbonate species very likely contributed to the more pronounced hysteresis [Tonnet et al., 2008; Broseta et al., 2012; Wang et al., 2012; Wang et al., 2013].

Unlike the results shown in the air-brine and decane-brine systems,  $S_{w,ir}$  values are of similar magnitude for quartz ( $S_{w,ir}$  of 0.03–0.05 ( $\Theta_{w,ir}$  of 0.012–0.019)) and limestone ( $S_{w,ir}$  of 0.04–0.07 ( $\Theta_{w,ir}$  of 0.015–0.028)) sands in the scCO<sub>2</sub>-brine system.  $S_{nw,r}$  ranged from 0.20 to 0.32 ( $\Theta_{nw,r}$  from 0.081 to 0.119) for quartz sand and from 0.12 to 0.32 ( $\Theta_{nw,r}$  from 0.041 to 0.117) for limestone sand. These results are similar to the values reported in literature [Pluq and Bruining, 2007; El-Maghraby and Blunt, 2013; Niu et al., 2015].

As previously mentioned, the deviations of the measured drainage and imbibition  $P_c$ – $S_w$  relations from the universal scaling inflections calculated with  $\lambda$  and  $\gamma$  (straight dash lines in Figures 5–7) indicate the interfacial properties in the multicomponent system have changed from the hydrophilic assumption. These deviations were attributed to wettability change [Tokunaga et al., 2013; Wang and Tokunaga, 2015] since the effect of  $\gamma$  has already been quantitatively accounted in  $\Pi_c$ , a  $\cos\theta$  term can be included to account for the rest of the difference (equation (3)). The effect of wettability on capillary trapping is well documented in literature [Suicmez et al., 2008; Al-Raoush, 2009; Zhao et al., 2010; Iglauer et al., 2015]. Fitting  $\Pi_c/\cos\theta$  with the characteristic scaling inflections permits evaluation of changes in both  $\gamma$  and  $\theta$ .

Assuming that  $\gamma$  is well constrained during the  $P_c$ – $S_w$  experiments for the multiple fluid pairs,  $\cos\theta$  and  $\theta$  values were calculated to compensate the deviation between the experimental results and the capillary scaling predictions. These values shed light on the extreme extent to which wettability might have altered and how significant capillary hysteresis ( $P_c$  difference between drainage and imbibition) and wettability hysteresis ( $\theta$  difference between advancing and receding processes) are.

Results obtained by matching the  $\Pi_c/\cos\theta$  curves with the characteristic scaling inflections for air-brine, decane-brine, and scCO<sub>2</sub>-brine fluid systems in quartz and limestone sands are shown in Figures (8 and 9), and 10, respectively. For air-brine, the calculated advancing/receding  $\theta$  (the upper and lower limits of wettability with equilibrium  $\theta$  bounding in between) values range from 35°–36°/0°–27° (quartz with DI water), 7°–10°/0° (quartz with brine), 32°–34°/23°–28° (limestone with brine), and 20°–27°/15°–20° (dolomite with brine), respectively. For decane-brine, the estimated advancing/receding (imbibition/drainage)  $\theta$  values range from 60.5°–62°/44.5°–50.4° (quartz) and 70.7°–73.3°/39°–47.9° (limestone), respectively. For scCO<sub>2</sub>-brine, the inferred advancing/receding (imbibition/drainage)  $\theta$  values range from 83.1°–84.8°/76.5°–77.3° (quartz) and 72.3°–85°/56°–68.6° (limestone), respectively. The  $\cos\theta$  and  $\theta$  values for all the experiments are listed in Table 2. These results are consistent with data in literature on dynamic contact angles, where advancing  $\theta$  in the imbibition events are greater than receding  $\theta$  values in the drainage events.

Postexperiment IFT measurements affirmed  $\gamma$  stayed unaltered during the experiments for air-brine and decane-brine experiments at RTP. The back-calculated  $\theta$  values for these experiments mentioned in the last paragraph and in Table 2 therefore reflect the realistic states of wettability. Exposure to air over the time scale of several months does not alter the wettability of the porous media. Both sandstone and carbonate sands remained hydrophilic. Wettability indeed gets altered to be less water-wetting after porous media being exposed to decane. In some cases, contact angles approached intermediate-wetting (70.7°–73.3°) but were still mostly in the moderately water-wetting range.

Scaling analysis with the results obtained from the scCO<sub>2</sub>-brine experiments at ETP indicated more significant wettability alteration (i.e., 83.1°–84.8°/76.5°–77.3° (quartz) and 72.3°–85°/56°–68.6° (limestone), in the intermediate-wetting range) compared with air-brine and decane-brine fluid pairs. It should be noted again that these inferred values were obtained based on the assumption that  $\gamma$  was well-constrained and the deviation from capillary scaling prediction was solely attributed to wettability alteration. They are qualitative indicators rather than precise contact angles within pores. Furthermore, these values are average representations of the wettability states of the entire sandpack and do not reflect possible grain-scale variation in wettability. It should also be noted that pore-lining and natural organic substances may play an important role on wettability alteration and capillary pressure [Heath et al., 2012].

As an important phenomenon in GCS, EOR, and vadose zone hydrology,  $S_{nw,r}$  (departure from complete water saturation at  $P_c \leq 0$ ) values were determined using accurate  $P_c$  control and  $S_w$  measurements in our RTP and ETP porous plate systems.  $S_{nw,r}$  was determined as the  $P_c$  was brought back to zero at the end of the imbibition experiments. This is different from the commonly employed method for determining  $S_{nw,r}$  involving increasingly driving  $P_c$  to usually unspecified negative values. The quantitation of  $S_{nw,r}$  at zero  $P_c$  best simulates the geological processes where imbibition plays a key role to drive brine to reoccupy the pore space and entrap the NWP.

The  $S_{nw,r}$  results for the air-brine, decane-brine, and scCO<sub>2</sub>-brine systems are summarized together in Figure 11. Note that  $\Theta_{nw,r}$  ( $\varphi S_{nw,r}$ , the volumetric brine content at the residual saturation) is equivalent to the capillary trapping capacity (as defined in Iglaue et al., [2011]) which is the volumetric fraction of trapped NWP relative to bulk volume of the porous media. Given the capillary-dominant regimes characterized by low capillary number, the entrapment of NWP is caused partly by snap-off at converging-diverging pore throats and interfacial phenomena including pinning and adhesion as shown in Figure 1, and partly by WP bypass engulfing NWP. Very low capillary trapping of air ( $S_{nw,r}$  of 0.04–0.09 ( $\Theta_{nw,r}$  from 0.014 to 0.035)) is observed in both silica and carbonate sands. Compared to silica sands ( $S_{nw,r}$  of 0.08–0.09 ( $\Theta_{nw,r}$  of 0.030–0.035) for quartz), carbonates show even lower residual air trapping ( $S_{nw,r}$  of 0.04–0.06 ( $\Theta_{nw,r}$  from 0.014 to 0.021) for limestone and dolomite). The residual decane trapping is generally higher than that of air in the same porous media. Carbonate shows greater  $S_{nw,r}$  values ( $S_{nw,r}$  of 0.15–0.18 ( $\Theta_{nw,r}$  of 0.051–0.060) for limestone) than sandstone ( $S_{nw,r}$  of 0.08–0.10 ( $\Theta_{nw,r}$  of 0.030–0.036) for quartz) which can be attributed to the greater affinity between CO<sub>2</sub> and carbonate species as previously noted. It should be noted that the  $S_{nw,r}$  values obtained from homogeneous unconsolidated porous media are not readily comparable with those obtained from consolidated porous media. The magnitude and trend of the results are complicated by capillary pressure heterogeneity, hysteresis, time and process-dependency, and mixed-wetting conditions [Basu and Sharma, 1996; Blunt, 1998; O'Carroll et al., 2005; Pini et al., 2012; Al-Menhali and Krevor, 2016].

Comparing between different fluid systems, the residual scCO<sub>2</sub> trapping is significantly higher than that of air and decane. The greater capillary trapping of scCO<sub>2</sub> relative to other nonwetting phases is consistent



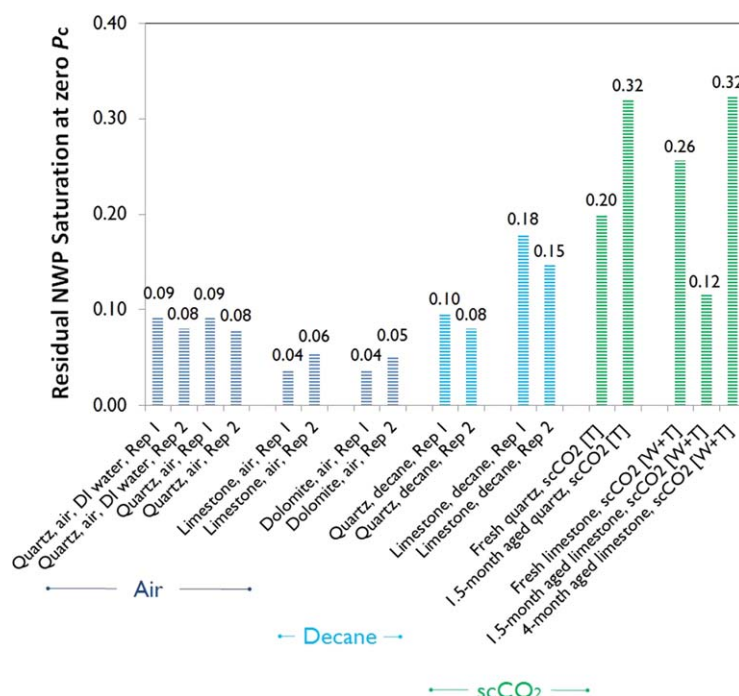


**Figure 11.** Measured residual NWP saturation,  $S_{nw,r}$  values for air, decane, and  $scCO_2$ . Unless mentioned otherwise, the WP is 1M NaCl synthetic brine.

with the results in some previous studies [Plug and Bruining, 2007; El-Maghraby and Blunt, 2013]. The amounts of residually trapped decane were also higher than those of air. We reiterate that the entrapment of fluid phases in the pore space is by nature the competition between invading and defending fluids of different physiochemical and interfacial properties. Given the identical properties of porous media in this study including pore structure, surface roughness, porosity, chemical and mineralogical composition, the differences in  $S_{nw,r}$  and  $\Theta_{nw,r}$  between different fluid pairs originate from the variant buoyancy (i.e., density difference), viscosity ratio, capillary pressure, IFT, wettability, and interfacial processes (e.g., adhesion/contact line pinning). Air is much more buoyant than decane and  $scCO_2$ , making its immobilization more difficult by the porous media. This resulted in the lowest  $S_{nw,r}$  and  $\Theta_{nw,r}$  for air amongst the three NWP fluids. This trend reaffirmed the conclusion that decreased density contrast resulted in greater NWP trapping [Morrow et al., 1988; Wang and Clarends, 2012; Suekane and Okada, 2013]. This trend could also be partly due to the differences in wettability states. A trend emerged suggesting that with wettability alteration toward the direction of less water-wetting by the NWP fluids (decane and  $scCO_2$  here),  $S_{nw,r}$  and  $\Theta_{nw,r}$  increased. Given that  $S_{nw,r}$  and  $\Theta_{nw,r}$  are a result of many physicochemical and interfacial properties/phenomena acting in synergy, whether wettability alteration is the main cause needs to be examined with further investigations.

Comparing between decane and  $scCO_2$ , although the buoyancy effect is very similar, results of capillary trapping were consistently different. Decane has been used as an analog fluid to  $scCO_2$  based on their similar properties, mainly density [Iglauder et al., 2011; Pentland et al., 2011]. Using decane as an analog fluid enabled simulation of multiple-component, multiple-phase  $scCO_2$ -brine experiments at ETP that are very challenging to conduct relative to experiments at RTP. The results here however indicate that the capillary behavior of decane fails to represent  $scCO_2$ , particularly with respect to emulating the important information of residual  $scCO_2$  trapping. The use of decane (possibly other analog fluids as well) generally underestimates  $S_{nw,r}$  and  $\Theta_{nw,r}$  for  $scCO_2$ . Differences in wettability states (more intermediate-wetting of  $scCO_2$  than decane) help to explain the differences in  $S_{nw,r}$  and  $\Theta_{nw,r}$  between the two NWPs.  $CO_2$  adhesion also very likely contributes to the higher  $S_{nw,r}$  and  $\Theta_{nw,r}$  for  $scCO_2$  [Wang et al., 2013]. The significantly distinct viscosity ratios between decane-brine and  $scCO_2$ -brine may play an important role as well [Wildenschild et al., 2011; Suekane and Okada, 2013]. Note from Table 1 that the viscosity ratio,  $\mu_r/\mu_w$ , of 0.85 for decane/brine is more than 10 times greater than that of  $scCO_2$ /brine. The much less viscous  $scCO_2$  has an unfavorably high mobility ratio compared to decane which exhibits a more piston-like pattern of displacement with brine that results in less trapped decane during imbibition.

These results have important implications for relating laboratory experiments to a variety of important multiphase fluid displacement processes in the field, including GCS, EOR, and vadose zone hydrology. The repeatedly measured drainage-imbibition cycles provide valuable information on the  $S_w$  responses to  $P_c$ , particularly in the main drainage and imbibition regions (i.e., significant change in  $S_w$  at its intermediate



levels). Given that most laboratory trapping studies rely on relatively fast spontaneous or forced imbibition, the  $S_{nw,r}$  data presented here with  $P_c = 0$  approached slowly provide new perspectives on residual NWP trapping under displacement rates relevant in the field. The porous plate method enabled direct measurements of changes in capillary and wettability behavior, and their hysteresis on an extended time scale (several months) thereby facilitating exploration of wettability alteration and changes in  $S_{nw,r}$ . Given that the fate and transport of NWPs are overall determined by the force balances between buoyancy, interfacial tension, and shear drag forces [Wildenschild *et al.*, 2011; Wang and Clarens, 2012; Suekane and Okada, 2013], these results help uncover the relative importance between different parameters. Moreover, capillary scaling facilitates evaluating the effects of interfacial properties which lays the foundation for future studies to separate and quantify the individual contributions of IFT and wettability to the deviated  $P_c$ - $S_w$  behaviors from predictions.

The decane-brine results provide a further look into the mechanism of EOR through imbibition. Wettability alteration of porous media materials induced by contact with decane is important. It contributes to slightly increased amounts of capillary trapped oil phase. Methods that help maintain a water-wetting reservoir would increase the amount of recovered oil. From another aspect, decane has been used as an analog fluid in GCS studies. However, this study revealed that decane is inadequate to predict  $\text{scCO}_2$  behavior in silicate and carbonate reservoirs. This is mainly due to the distinct differences in wettability characteristics and viscosity ratio (and thus mobility ratio). The time-dependent behavior of  $\text{scCO}_2$ -water cannot be captured in analog decane-water experiments. Although more technically challenging, experiments concerned with multiphase behavior in GCS reservoirs are best conducted with  $\text{scCO}_2$  under conditions representing reservoir pressures and temperatures.

#### 4. Conclusions

We systematically characterized the  $P_c$ - $S_w$  relations of air-brine, oil (decane)-brine, and  $\text{scCO}_2$ -brine fluid systems in silica (quartz) and carbonate (limestone and dolomite) sands using three custom-built porous plate experimental systems under ambient and reservoir conditions. This investigation enabled us to study the equilibrium capillary and NWP entrapment phenomena. The  $\text{scCO}_2$ -brine fluid pair has the highest  $S_{nw,r}$  followed by decane-brine. Air-brine has the lowest  $S_{nw,r}$ . The  $P_c$ - $S_w$  curves of decane-brine and  $\text{scCO}_2$ -brine deviated significantly from capillary scaling predictions and shifted toward lower  $P_c$ . The shifted curves indicated significant wettability alteration of porous media toward weakly water-wetting compared with air-brine. The flow and displacement regimes, and residual trapping are complicated by interfacial phenomena including the behavior of water films as illustrated in Figure 1. The differences between decane-brine and  $\text{scCO}_2$ -brine  $P_c$ - $S_w$  results also indicate that using decane as the surrogate for  $\text{scCO}_2$  underpredicts its residual trapping. Therefore, ETP experiments with  $\text{scCO}_2$  remain necessary to directly measure capillary and interfacial behavior of GCS reservoirs. This work is also important for understanding longer term  $\text{CO}_2$  behavior during GCS, with particular relevance to the postinjection stage where  $\text{scCO}_2$  remains nearly stagnant in pore spaces, and is capillary trapped under  $P_c \approx 0$ . The cyclic  $P_c$ - $S_w$  drainage and imbibition events in  $\text{scCO}_2$ -brine over several months collectively indicated that wettability alteration over time may facilitate larger amounts of  $\text{scCO}_2$  storage in reservoirs and greater contribution to mitigation of climate change caused by  $\text{CO}_2$  emissions.

#### Acknowledgments

This work was supported as part of the Center for Nanoscale Controls on Geologic  $\text{CO}_2$  (NCGC), an Energy Frontier Research Center funded by the U.S. Department of Energy, Office of Science, Basic Energy Sciences under Award # DE-AC02-05CH11231. The data used are listed in the references, tables, and figures. We thank the anonymous reviewers, Associate Editor Markus Hilpert, and Editor Hari Rajaram for their helpful comments.

#### References

- Aissaoui, A. (1983), Etude théorique et expérimentale de l'hystérésis des pressions capillaires et des perméabilités relatives en vue du stockage souterrain de gaz, PhD thesis, Ecole des Mines de Paris, Paris, France.
- Al Mansoori, S. K., S. Iglaer, C. H. Pentland, and M. J. Blunt (2009), Three-phase measurements of oil and gas trapping in sand packs, *Adv. Water Resour.*, 32(10), 1535–1542.
- Al-Menhali, A. S., and S. Krevor (2016), Capillary trapping of  $\text{CO}_2$  in oil reservoirs: Observations in a mixed-wet carbonate rock, *Environ. Sci. Technol.*, 50(5), 2727–2734.
- Al-Raoush, R. I. (2009), Impact of wettability on pore-scale characteristics of residual nonaqueous phase liquids, *Environ. Sci. Technol.*, 43(13), 4796–4801.
- Anderson, W. G. (1987), Wettability literature survey-Part 4: Effects of wettability on capillary pressure, *J. Pet. Technol.*, 39(10), 1283–1300.
- Andrew, M., B. Bijeljic, and M. J. Blunt (2014), Pore-scale imaging of trapped supercritical carbon dioxide in sandstones and carbonates, *Int. J. Greenhouse Gas Control*, 22, 1–14.
- Bachu, S., and D. B. Bennion (2009), Dependence of  $\text{CO}_2$ -brine interfacial tension on aquifer pressure, temperature and water salinity, *Energy Procedia*, 1(1), 3157–3164.

- Basu, S., and M. M. Sharma (1996), Measurement of critical disjoining pressure for dewetting of solid surfaces, *J. Colloid Interface Sci.*, **181**(2), 443–455.
- Batzle, M. and Z. Wang (1992), Seismic properties of pore fluids, *Geophysics*, **57**(11), 1396–1408.
- Benson, S. M., and D. R. Cole (2008), CO<sub>2</sub> sequestration in deep sedimentary formations, *Elements*, **4**, 325–331.
- Berg, S., et al. (2013a), Real-time 3D imaging of Haines jumps in porous media flow, *Proc. Natl. Acad. Sci. U. S. A.*, **110**(10), 3755–3759.
- Berg, S., S. Oedai, and H. Ott (2013b), Displacement and mass transfer between saturated and unsaturated CO<sub>2</sub>-brine systems in sandstone, *Int. J. Greenhouse Gas Control*, **12**, 478–492.
- Blunt, M. J. (1998), Physically-based network modeling of multiphase flow in intermediate-wet porous media, *J. Pet. Sci. Eng.*, **20**(3), 117–125.
- Blunt, M. J., B. Bijeljic, H. Dong, O. Gharbi, S. Iglauer, P. Mostaghimi, A. Paluszny, and C. Pentland (2013), Pore-scale imaging and modelling, *Adv. Water Resour.*, **51**, 197–216.
- Broseta, D., N. Tonnet, and V. Shah (2012), Are rocks still water-wet in the presence of dense CO<sub>2</sub> or H<sub>2</sub>S?, *Geofluids*, **12**(4), 280–294.
- Buckley, J. S., K. Takamura, and N. R. Morrow (1989), Influence of electrical surface charges on the wetting properties of crude oils, *SPE Reservoir Eng.*, **4**(3), 332–340.
- Bull, Ø., F. Bratteli, J. K. Ringen, K. Melhuus, A. L. Bye, and J. E. Iversen (2011), The quest for the true residual gas saturation—An experimental approach, in *Society of Core Analysts Symposium, SCA2011-03*, Austin, Tex.
- Celia, M. A., P. C. Reeves, and L. A. Ferrand (1995), Recent advances in pore scale models for multiphase flow in porous media, *Rev. Geophys.*, **33**(S2), 1049–1057.
- Chaudhary, K., B. M. Cardenas, W. W. Wolfe, J. A. Maisano, R. A. Ketcham, and P. C. Bennett (2013), Pore-scale trapping of supercritical CO<sub>2</sub> and the role of grain wettability and shape, *Geophys. Res. Lett.*, **40**, 3878–3882, doi:10.1002/grl.50658.
- Deng, W., M. B. Cardenas, and P. C. Bennett (2014), Extended Roof snap-off for a continuous nonwetting fluid and an example case for supercritical CO<sub>2</sub>, *Adv. Water Resour.*, **64**, 34–46.
- El-Maghraby, R. M., and M. J. Blunt (2013), Residual CO<sub>2</sub> trapping in Indiana limestone, *Environ. Sci. Technol.*, **47**(1), 227–233.
- Enick, R. M., D. K. Olsen, J. R. Ammer, and W. Schuller (2012), Mobility and conformance control for CO<sub>2</sub> EOR via thickeners, foams, and gels—a literature review of 40 years of research and pilot tests, in *SPE Improved Oil Recovery Symposium*, Soc. of Pet. Eng., Tulsa, Okla.
- Farajzadeh, R., A. Andrianov, R. Krastev, G. J. Hirasaki, and W. R. Rossen (2012), Foam-oil interaction in porous media: Implications for foam assisted enhanced oil recovery, *Adv. Colloid Interface Sci.*, **183**, 1–13.
- Faybishenko, B. A. (1995), Hydraulic behavior of quasi-saturated soils in the presence of entrapped air: Laboratory experiments, *Water Resour. Res.*, **31**(10), 2421–2435.
- Geistlinger, H., S. Mohammadian, S. Schlueter, and H. J. Vogel (2014), Quantification of capillary trapping of gas clusters using X-ray microtomography, *Water Resour. Res.*, **50**, 4514–4529, doi:10.1002/2013WR014657.
- Gittins, P., S. Iglauer, C. H. Pentland, S. Al-Mansoori, S. Al-Sayari, B. Bijeljic, and M. J. Blunt (2010), Nonwetting phase residual saturation in sand packs, *J. Porous Media*, **13**(7), 591–599.
- Haines, W. B. (1930), Studies in the physical properties of soil: V. The hysteresis effect in capillary properties, and the modes of moisture distribution associated therewith, *J. Agric. Sci.*, **20**, 97–116.
- Heath, J. E., T. A. Dewers, B. J. McPherson, M. B. Nemer, and P. G. Kotula (2012), Pore-lining phases and capillary breakthrough pressure of mudstone caprocks: Sealing efficiency of geologic CO<sub>2</sub> storage sites, *Int. J. Greenhouse Gas Control*, **11**, 204–220.
- Hilfer, R. (1996), Transport and relaxation phenomena in porous media, *Adv. Chem. Phys.*, **92**, 299–424.
- Hong, S. J., F. M. Chang, T. H. Chou, S. H. Chan, Y. J. Sheng, and H. K. Tsao (2011), Anomalous contact angle hysteresis of a captive bubble: Advancing contact line pinning, *Langmuir*, **27**(11), 6890–6896.
- Iglauer, S., W. Wulling, C. H. Pentland, S. K. Al-Mansoori, and M. J. Blunt (2011), Capillary-trapping capacity of sandstones and sandpacks, *Soc. Pet. Eng. J.*, **16**(4), 778–783.
- Iglauer, S., C. H. Pentland, and A. Busch (2015), CO<sub>2</sub> wettability of seal and reservoir rocks and the implications for carbon geo-sequestration, *Water Resour. Res.*, **51**, 729–774, doi:10.1002/2014WR015553.
- Intergovernmental Panel on Climate Change (2005), Underground geological storage, in *IPCC Special Report on Carbon Dioxide Capture and Storage*, pp. 195–276, Cambridge Univ. Press, Cambridge.
- Jost, D., C. M. Haberer, P. Grathwohl, J. Winter, and C. Gallert (2015), Oxygen transfer in a fluctuating capillary fringe: Impact of microbial respiratory activity, *Vadose Zone J.*, **14**(5), 1–14.
- Kantzas, A., M. Ding, and J. Lee (2000), Residual gas saturation revisited, In *SPE/CERI Gas Technology Symposium*, Soc. of Petrol. Eng.
- Kendall, K. (1994), Adhesion: Molecules and mechanics, *Science*, **263**(5154), 1720–1725.
- Kestin, J., H. E. Khalifa, and R. J. Correia (1981), Tables of the dynamic and kinematic viscosity of aqueous NaCl solutions in the temperature range 20–150 C and the pressure range 0.1–35 MPa, *J. Phys. Chem. Ref. Data*, **10**(1), 71–88.
- Klute, A., and G. E. Wilkinson (1958), Some tests of the similar media concept of capillary flow: 1. Reduced capillary conductivity and moisture characteristic data, *Soil Sci. Soc. Am. J.*, **22**, 278–281.
- Krevor, S., M. J. Blunt, S. M. Benson, C. H. Pentland, C. Reynolds, A. Al-Menhali, and B. Niu (2015), Capillary trapping for geologic carbon dioxide storage—From pore scale physics to field scale implications, *Int. J. Greenhouse Gas Control*, **40**, 221–237.
- Land, C. S. (1968), Calculation of imbibition relative permeability for two- and three-phase flow from rock properties, *Trans. Metall. Soc. AIME*, **243**, 149–156.
- Lemmon, E. W., and R. T. Jacobsen (2004), Viscosity and thermal conductivity equations for nitrogen, oxygen, argon, and air, *Int. J. Thermophys.*, **25**(1), 21–69.
- Leverett, M. C. (1941), Capillary behavior in porous solids, *Trans. Metallurg. Soc. AIME*, **142**, 152–169.
- Mason, G. and N. R. Morrow (2013), Developments in spontaneous imbibition and possibilities for future work, *J. Pet. Sci. Eng.*, **110**, 268–293.
- Miller, E. E., and R. D. Miller (1956), Physical theory for capillary flow phenomena, *J. Appl. Phys.*, **4**, 324–332.
- Mori, H., T. Sakaki, and T. H. Illangasekare (2015), Laboratory study of geological carbon sequestration using surrogate fluids: Dielectric measurement and scaling of capillary pressure-saturation relationships, *Int. J. Greenhouse Gas Control*, **37**, 146–157.
- Morrow N.R., I. Chatzis, and J.T. Taber (1988), Entrapment and mobilization of residual oil in bead packs, *Soc. Pet. Eng. Reservoir Eng.*, **3**, 927–934.
- National Institute of Standards and Technology (2016), Web-based database. [Available at <http://webbook.nist.gov/chemistry/fluid/>]
- Niu, B., A. Al-Menhali, and S. C. Krevor (2015), The impact of reservoir conditions on the residual trapping of carbon dioxide in Berea sandstone, *Water Resour. Res.*, **51**, 2009–2029, doi:10.1002/2014WR016441.

- O'Carroll, D. M., L. M. Abriola, C. A. Polityka, S. A. Bradford, and A. H. Demond (2005), Prediction of two-phase capillary pressure-saturation relationships in fractional wettability systems, *J. Contam. Hydrol.*, **77**(4), 247–270.
- Parker, J. C., R. J. Lenhard, and T. Kuppusamy (1987), A parametric model for constitutive properties governing multiphase flow in porous media, *Water Resour. Res.*, **23**(4), 618–624.
- Pentland, C. H., S. Al-Mansoori, S. Iglauer, B. Bijeljic, and M. J. Blunt (2010), Measurement of non-wetting phase trapping in sand packs, *Soc. of Petrol. Eng. J.*, **15**(2), 274–281.
- Pentland, C. H., R. El-Maghraby, S. Iglauer, and M. J. Blunt (2011), Measurements of the capillary trapping of super-critical carbon dioxide in Berea sandstone, *Geophys. Res. Lett.*, **38**, L06401, doi:10.1029/2011GL046683.
- Philip, J. R. (1971), Limitations on scaling by contact angle, *Soil Sci. Soc. Am. Proc.*, **35**, 507–509.
- Pini, R., S. Krevor, and S. M. Benson (2012), Capillary pressure and heterogeneity for the CO<sub>2</sub>/water system in sandstone rocks at reservoir conditions, *Adv. Water Resour.*, **38**, 48–59.
- Plug, W. J., and J. Bruining (2007), Capillary pressure for the sand-CO<sub>2</sub>-water system under various pressure conditions. Application to CO<sub>2</sub> sequestration, *Adv. Water Resour.*, **30**(11), 2339–2353.
- Roof, J. G. (1970), Snap-off of oil droplets in water-wet pores, *Soc. Pet. Eng. J.*, **10**(1), 85–90.
- Sakaki, T., P. E. Schulte, A. Cihan, J. A. Christ, and T. H. Illangasekare (2013), Airflow pathway development as affected by soil moisture variability in heterogeneous soils, *Vadose Zone J.*, **12**(1), 1–14.
- Schroth, M. H., S. J. Ahearn, J. S. Selker, and J. D. Istok (1996), Characterization of Miller-similar silica sands for laboratory hydrologic studies, *Soil Sci. Soc. of Am. J.*, **60**, 1331–1339.
- Suekane, T., and K. Okada (2013), Gas injection in a water saturated porous medium: Effect of capillarity, buoyancy, and viscosity ratio, *Energy Procedia*, **37**, 5545–5552.
- Suicmez, V. S., M. Piri, and M. J. Blunt (2008), Effects of wettability and pore-level displacement on hydrocarbon trapping, *Adv. Water Resour.*, **31**(3), 503–512.
- Suzanne, K., G. Hamon, J. Billiotte, and V. Trocme (2003), Experimental relationships between residual gas saturation and initial gas saturation in heterogeneous sandstone reservoirs, in *SPE Annual Technical Conference and Exhibition*, Soc. of Pet. Eng., Denver, Colo.
- Tanino, Y., and M. J. Blunt (2013), Laboratory investigation of capillary trapping under mixed-wet conditions, *Water Resour. Res.*, **49**(7), 4311–4319.
- Tokunaga, T. K., and J. Wan (2013), Capillary pressure and mineral wettability influences on reservoir CO<sub>2</sub> capacity, *Rev. Mineral. Geochem.*, **77**(1), 481–503.
- Tokunaga, T. K., J. Wan, J. W. Jung, T. W. Kim, Y. Kim, and W. Dong (2013), Capillary pressure and saturation relations for supercritical CO<sub>2</sub> and brine in sand: High-pressure P<sub>c</sub>(S<sub>w</sub>) controller/meter measurements and capillary scaling predictions, *Water Resour. Res.*, **49**, 4566–4579, doi:10.1002/wrcr.20316.
- Tonnet, N., V. Shah, P. Chiquet, J. Diaz, G. Mouronval, and D. Broseta (2008), Wettability alteration of caprock minerals by acid gases, in *10th International Symposium on Reservoir Wettability*, Abu Dhabi, United Arab Emirates.
- Tutolo, B. M., A. J. Luhmann, X. Z. Kong, M. O. Saar, and W. E. Seyfried Jr (2014), Experimental observation of permeability changes in dolomite at CO<sub>2</sub> sequestration conditions, *Environ. Sci. Technol.*, **48**(4), 2445–2452.
- Valvatne, P. H., and M. J. Blunt (2004), Predictive pore-scale modeling of two-phase flow in mixed wet media, *Water Resour. Res.*, **40**, W07406, doi:10.1029/2003WR002627.
- van Genuchten, M. T. (1980), A closed-form equation for predicting the hydraulic conductivity of unsaturated soils, *Soil Sci. Soc. Am. J.*, **44**(5), 892–898.
- Wang, S., and A. F. Clarens (2012), The effects of CO<sub>2</sub>-brine rheology on leakage processes in geologic carbon sequestration, *Water Resour. Res.*, **48**, W08518, doi:10.1029/2011WR011220.
- Wang, S., and T. K. Tokunaga (2015), Capillary pressure-saturation relations for supercritical CO<sub>2</sub> and brine in limestone/dolomite sands: Implications for geologic carbon sequestration in carbonate reservoirs, *Environ. Sci. Technol.*, **49**(12), 7208–7217.
- Wang, S., I. M. Edwards, and A. F. Clarens (2012), Wettability phenomena at the CO<sub>2</sub>-brine-mineral interface: Implications for geologic carbon sequestration, *Environ. Sci. Technol.*, **47**(1), 234–241.
- Wang, S., Z. Tao, S. M. Persily, and A. F. Clarens (2013), CO<sub>2</sub> adhesion on hydrated mineral surfaces, *Environ. Sci. Technol.*, **47**(20), 11,858–11,865.
- Wildenschild, D., R. T. Armstrong, A. L. Herring, I. M. Young, and J. W. Carey (2011), Exploring capillary trapping efficiency as a function of interfacial tension, viscosity, and flow rate, *Energy Procedia*, **4**, 4945–4952.
- Yang, S. H., and R. L. Reed (1989), Mobility control using CO<sub>2</sub> foams, in *SPE Annual Technical Conference and Exhibition*, Soc. of Pet. Eng., San Antonio, Tex.
- Zhao, X., M. J. Blunt, and J. Yao (2010), Pore-scale modeling: Effects of wettability on waterflood oil recovery, *J. Pet. Sci. Eng.*, **71**(3), 169–178.



*Water Resources Research*

Supporting Information for

**Capillary Pressure — Saturation Relations in Quartz and Carbonate Sands: Limitations for Correlating Capillary and Wettability Influences on Air, Oil, and Supercritical CO<sub>2</sub> Trapping**

Shibo Wang, Tetsu K. Tokunaga, Jiamin Wan, Wenming Dong, Yongman Kim

Energy Geosciences Division, Lawrence Berkeley National Laboratory, Berkeley, California, USA

**Contents of this file**

Text S1 to S3

Tables S1 to S2

## S1 Experimental Conditions

Seventeen groups of experiments were conducted with the four fluid pairs of the three fluid systems and in quartz, limestone, and dolomite sands under RTP and ETP conditions.

**Table S1.** Experimental Conditions Investigated in This Work

Index	Temperature, °C	Pressure, MPa	Fluid Pair	Mineral	Processes	Replicate
1	23	0.1	#1	quartz sand	drainage & imbibition	1
2	23	0.1	#1	quartz sand	drainage & imbibition	2
3	23	0.1	#2	quartz sand	drainage & imbibition	1
4	23	0.1	#2	quartz sand	drainage & imbibition	2
5	23	0.1	#2	limestone sand	drainage & imbibition	1
6	23	0.1	#2	limestone sand	drainage & imbibition	2
7	23	0.1	#2	dolomite sand	drainage & imbibition	1
8	23	0.1	#2	dolomite sand	drainage & imbibition	2
9	23	0.1	#3	quartz sand	drainage & imbibition	1
10	23	0.1	#3	quartz sand	drainage & imbibition	2
11	23	0.1	#3	limestone sand	drainage & imbibition	1
12	23	0.1	#3	limestone sand	drainage & imbibition	2
13 <sup>a</sup>	45	12	#4	quartz sand	drainage & imbibition	1
14 <sup>a</sup>	45	12	#4	quartz sand	drainage & imbibition	2
15 <sup>b</sup>	45	12	#4	limestone sand	drainage & imbibition	1
16 <sup>b</sup>	45	12	#4	limestone sand	drainage & imbibition	2
17 <sup>b</sup>	45	12	#4	limestone sand	drainage & imbibition	3

<sup>a</sup>These conditions were studied in our previous work [Tokunaga *et al.*, 2013].

<sup>b</sup>These conditions were studied in our previous work [Wang and Tokunaga, 2015].



## S2 Fitting Parameters of *van Genuchten* Model

**Table S2.** Fitting Parameters of *van Genuchten* Model (Equation 4) for the Drainage and Imbibition Curves (Figure 6, 7 and 8)<sup>a</sup>

		$\Theta_s$	$S_s$	$\Theta_r$	$S_r$	$\alpha$ (Pa <sup>-1</sup> )	n	m
Air—water—quartz—1 (#1) <sup>b</sup>	Drainage	0.380	1.00	0.059	0.15	$3.61 \times 10^{-4}$	20.68	0.29
	Imbibition	0.345	0.91	0.059	0.15	$8.99 \times 10^{-4}$	10.27	0.21
Air—water—quartz—2 (#2) <sup>b</sup>	Drainage	0.346	0.91	0.061	0.16	$4.56 \times 10^{-4}$	6.58	0.52
	Imbibition	0.349	0.92	0.061	0.16	$9.19 \times 10^{-4}$	9.31	0.18
Air—brine—quartz—1 (#3) <sup>b</sup>	Drainage	0.380	1.00	0.061	0.16	$3.57 \times 10^{-4}$	25.35	0.33
	Imbibition	0.345	0.91	0.061	0.16	$5.82 \times 10^{-4}$	8.91	0.51
Air—brine—quartz—2 (#4) <sup>b</sup>	Drainage	0.350	0.92	0.065	0.17	$3.61 \times 10^{-4}$	10.61	0.67
	Imbibition	0.350	0.92	0.065	0.17	$4.74 \times 10^{-4}$	4.90	1.47
Air—brine—limestone—1 (#5) <sup>b</sup>	Drainage	0.380	1.00	0.015	0.04	$4.09 \times 10^{-4}$	26.85	0.26
	Imbibition	0.366	0.96	0.015	0.04	$7.15 \times 10^{-4}$	7.50	0.45
Air—brine—limestone—2 (#6) <sup>b</sup>	Drainage	0.369	0.97	0.015	0.04	$4.09 \times 10^{-4}$	10.30	0.68
	Imbibition	0.359	0.94	0.015	0.04	$6.32 \times 10^{-4}$	4.60	0.95
Air—brine—dolomite—1 (#7) <sup>b</sup>	Drainage	0.380	1.00	0.015	0.04	$3.91 \times 10^{-4}$	21.45	0.35
	Imbibition	0.366	0.96	0.015	0.04	$6.54 \times 10^{-4}$	8.64	0.43
Air—brine—dolomite—2 (#8) <sup>b</sup>	Drainage	0.366	0.96	0.023	0.06	$3.95 \times 10^{-4}$	12.98	0.55
	Imbibition	0.361	0.95	0.023	0.06	$5.67 \times 10^{-4}$	5.61	1.03
Decane—brine—quartz—1 (#9) <sup>b</sup>	Drainage	0.380	1.00	0.088	0.23	$7.61 \times 10^{-4}$	6.86	0.82
	Imbibition	0.344	0.90	0.088	0.23	$1.25 \times 10^{-3}$	2.93	1.67
Decane—brine—quartz—2 (#10) <sup>b</sup>	Drainage	0.357	0.94	0.087	0.23	$4.72 \times 10^{-4}$	3.73	5.76
	Imbibition	0.350	0.92	0.087	0.23	$1.58 \times 10^{-4}$	2.03	85.67
Decane—brine—limestone—1 (#11) <sup>b</sup>	Drainage	0.380	1.00	0.011	0.03	$4.54 \times 10^{-4}$	5.99	7.99
	Imbibition	0.335	0.88	0.011	0.03	$5.62 \times 10^{-5}$	1.21	74.51
Decane—brine—limestone—2 (#12) <sup>b</sup>	Drainage	0.346	0.91	0.013	0.03	$6.89 \times 10^{-4}$	22.14	8.46
	Imbibition	0.332	0.87	0.013	0.03	$6.64 \times 10^{-5}$	1.23	74.51
12.0 MPa CO <sub>2</sub> —brine—quartz—1 (#13) <sup>b</sup>	Drainage	0.380	1.00	0.019	0.05	$9.08 \times 10^{-4}$	2.89	143.36
	Imbibition	0.299	0.79	0.019	0.05	$4.83 \times 10^{-4}$	1.70	85.67
12.0 MPa CO <sub>2</sub> —brine—quartz—2 (#14) <sup>b</sup>	Drainage	0.315	0.83	0.013	0.03	$6.06 \times 10^{-4}$	2.35	143.37
	Imbibition	0.261	0.69	0.013	0.03	$4.24 \times 10^{-4}$	1.62	85.67
12.0 MPa CO <sub>2</sub> —brine—limestone—1 (#15) <sup>b</sup>	Drainage	0.380	1.00	0.015	0.04	$1.59 \times 10^{-3}$	19.24	0.47
	Imbibition	0.284	0.75	0.015	0.04	$1.06 \times 10^{-3}$	2.25	33.61
12.0 MPa CO <sub>2</sub> —brine—limestone—2 (#16) <sup>b</sup>	Drainage	0.380	1.00	0.016	0.04	$2.54 \times 10^{-3}$	46.82	0.13
	Imbibition	0.339	0.89	0.015	0.04	$5.74 \times 10^{-4}$	2.30	74.64
12.0 MPa CO <sub>2</sub> —brine—limestone—3 (#17) <sup>b</sup>	Drainage	0.380	1.00	0.028	0.07	$1.71 \times 10^{-3}$	3.92	2.61
	Imbibition	0.263	0.69	0.028	0.07	$1.76 \times 10^{-2}$	3.27	0.58

<sup>a</sup>Note that curves were fitted to minimize root-mean-square deviations to the full drainage or imbibition curves instead of forcing through data at  $P_c = 0$ .

<sup>b</sup>The numbers in the parenthesis correspond to the experimental conditions listed in Table S1.

### S3 References

1. Tokunaga, T. K.; Wan, J.; Jung, J. W.; Kim, T. W.; Kim, Y.; Dong, W. Capillary pressure and saturation relations for supercritical CO<sub>2</sub> and brine in sand: High-pressure  $P_c(S_w)$  controller/meter measurements and capillary scaling predictions. *Water Resources Research* 2013, 49(8), 4566-4579.
2. Wang, S.; Tokunaga, T.K. Capillary pressure–saturation relations for supercritical CO<sub>2</sub> and brine in limestone/dolomite sands: Implications for geologic carbon sequestration in carbonate reservoirs. *Environmental Science & Technology* 2015, 49(12), 7208-7217.